Icosahedral Short-Range Order Suppresses Thermal Expansion in Metallic Glasses

Hajar Boutnala,[1,*] Hayat Haouas,[2] Achraf Atila,[3,†] and Abdellatif Hasnaoui[1,‡]

[1] *LS2ME Laboratory, Sultan Moulay Slimane University of Beni Mellal, Polydisciplinary faculty of Khouribga, B.P. 145, 25000 Khouribga, Morocco*

[2] *Laboratory of Inorganic Materials for Sustainable Energy Technologies (LIMSET), Mohammed VI Polytechnic University (UM6P), Benguerir 43150, Morocco*

[3] *Federal Institute of Materials Research and Testing (BAM), Unter den Eichen 87, Berlin 12205, Germany*

(Dated: June 29, 2026)

Understanding the structural origins of thermal expansion in metallic glasses (MGs) is essential for engineering next-generation materials with high thermal stability and performance. Accordingly, we used molecular dynamics simulations to investigate how local atomic motifs control the thermal expansion of MGs. Motif-resolved analysis using Voronoi tessellation reveals that mixed polyhedra are the main contributors to macroscopic thermal expansion, whereas icosahedral units act as stabilizers that resist volume changes. This interpretation is supported by motif-resolved potential-energy analysis, which shows lower, more temperature-stable energies for icosahedral polyhedra, in contrast to the strongly anharmonic response of mixed polyhedra. To connect motif-level thermal expansion to atomic-scale behavior, we analyzed bonds using the radial probability function ($G(r)$). A skewed-normal fit to the first peak shows a monotonic increase in mean interatomic distance with temperature, resolving the apparent contraction reported in earlier studies relying solely on the position of the first peak of $G(r)$. Overall, this work establishes a coherent structural picture for thermal expansion in MGs. The consistent behavior across the investigated alloys demonstrates that icosahedral units are systematically associated with lower local expansion, while mixed polyhedra dominate the macroscopic thermal response. This motif-dependent behavior is robust across different compositions, interatomic potentials, and cooling rates, providing a basis for designing MGs with improved thermal stability.

I. INTRODUCTION

Unlike crystalline metals, which have an ordered structure, metallic glasses (MGs) inherit the disordered structure of liquids through rapid quenching. Consequently, they lack long-range order and crystalline defects such as grain boundaries and dislocations, exhibiting instead an amorphous structure characterized by short-range order (SRO) and medium-range order (MRO) [1–4]. This distinctive structure underpins the exceptional properties of MGs, including high yield strength, large elastic limits, low Young's modulus [5, 6], excellent corrosion resistance [7], soft magnetic behavior [8, 9], high wear resistance [10, 11], and promising electrocatalytic performance [12–14]. These attributes make MGs attractive for applications ranging from structural components to biomedical and energy systems [15–19].

Temperature variations induce dimensional changes in materials, generating thermal strains and stresses that are critical during high temperature processing and service [20]. Such effects play a central role in solid-state forming processes and solidification routes, where uncontrolled thermal stresses can lead to residual stresses or cracking [21, 22]. Consequently, for MGs to be effectively utilized in applications such as aerospace components, automotive parts, and electronic devices, a comprehensive understanding of their thermal behavior, particularly thermal expansion, is crucial. For instance, in aerospace, materials must withstand extreme temperature variations without significant deformation or failure [23].

Thermal expansion, quantified by the coefficient of thermal expansion (CTE) $\beta = \frac{1}{V}\left(\frac{\partial V}{\partial T}\right)_P$, where V is the materials volume, T is the temperature, and P is the pressure, originates from the anharmonicity of interatomic potentials [24]. In metallic glasses, the anharmonicity of interatomic interactions manifests heterogeneously due to the broad distribution of local atomic environments [25, 26]. While crystalline materials typically exhibit uniform thermal expansion governed by a single, well-defined bonding environment, glasses possess a wide distribution of local atomic configurations. As a result, their thermal expansion behavior is inherently more complex and reflects the collective response of diverse local environments [27–30].

Indeed, experimental techniques, including differential and interferometric dilatometry, and strain-gauge measurements, have provided valuable insights into the thermal expansion of metallic liquids and glasses [31–34]. Molecular dynamics (MD) simulations offer a complementary approach by directly tracking temperature-induced dimensional changes at the atomic scale [35]. Recent studies have further demonstrated that thermal expansion in MGs is spatially heterogeneous, with local fluctuations in CTE generating internal stresses that may activate shear transformations [30]. Synchrotron X-ray diffraction experiments corroborate these findings, revealing scale-dependent thermal strains associated with

* hajar.boutnala@usms.ac.ma
† achraf.atila@bam.de
‡ hasnaoui59@hotmail.com

local rearrangements in SRO [36].

Despite these advances, local CTEs in MGs are commonly estimated from temperature-dependent peak positions of the radial distribution function. This approach often yields values that deviate from macroscopic measurements and may even suggest negative expansion in the first coordination shell [37–42]. Such apparent contraction does not reflect true bond shortening but arises from asymmetric peak shapes, which bias bond-length estimates based on the position of the first peak of the radial distribution function. These limitations underscore the need for alternative, structurally consistent methods to quantify local thermal expansion and to link macroscopic behavior to atomic-scale mechanisms. In particular, the role of distinct atomic motifs, such as icosahedral and mixed polyhedral environments, remains largely unexplored.

In this work, we investigate the structural and thermal expansion behavior of Ni- and Fe-based MGs using MD simulations. These systems are of particular interest due to their favorable magnetic, mechanical, and corrosion-resistant properties [8, 43–45]. Local CTEs are determined from the temperature-dependent atomic volumes of distinct Voronoi polyhedra below and above the glass transition temperature (T_g). Additionally, local bond expansion is investigated by tracking the evolution of the mean nearest-neighbor distance from the radial probability function.

II. METHODS

Molecular dynamics simulations were performed using the Large-scale Atomic/Molecular Massively Parallel Simulator (LAMMPS) software [46] to investigate the structural and thermodynamic properties of both monatomic (Fe, Al, Ni) and alloyed MGs. The studied alloyed systems include binary ($Fe_{75}Ni_{25}$, $Fe_{50}Ni_{50}$, $Fe_{25}Ni_{75}$, $Ni_{75}Al_{25}$, $Ni_{80}Al_{20}$, $Ni_{70}Al_{30}$), ternary alloys ($Fe_{50}Cu_{20}Ni_{30}$, $Fe_{40}Cu_{40}Ni_{20}$, $Fe_{40}Cu_{30}Ni_{30}$, $Fe_{60}Ni_{25}Cr_{15}$, $Fe_{60}Ni_{30}Cr_{10}$, $Fe_{60}Ni_{30}Co_{10}$, $Ni_{70}Al_{20}Co_{10}$, $Ni_{80}Al_{5}Co_{15}$, $Ni_{80}Al_{10}Co_{10}$, $Ni_{80}Al_{15}Co_{5}$, $Ni_{60}Al_{30}Co_{10}$, $Ni_{50}Al_{30}Co_{20}$), the medium entropy alloy (MEA) $Fe_{50}Ni_{30}Co_{10}Cr_{10}Mn_{10}$, rare-earth-based systems (Sm_4Al_{96} and $Sm_{10}Al_{90}$), and $Cu_{65}Zr_{35}$ metallic glasses modeled using both machine-learning and EAM potentials.

The interatomic potential is a key component in atomic simulations, as it determines the interactions between atoms and defines how the potential energy of a system varies with their positions. To describe interactions in Al, Ni, Ni-Al, and Ni-Al-Co systems, we adopted the Embedded-Atom Method (EAM) potential developed by Pun *et al.* [47]. This potential successfully replicates the martensitic phase transformation in ferromagnetic shape memory alloys of the Ni-Al-Co system and has been widely employed for modeling MGs [6, 48–51]. Namely, it has been used to examine the local structural configuration of the amorphous $Ni_{50}Al_{45}Co_5$ alloy system under uniaxial tensile deformation [48]. In the EAM formalism, the total energy of the system is expressed as [52]:

$$E_{\text{tot}} = \sum_i F_i(\rho_i) + \frac{1}{2}\sum_{i\neq j}\phi_{ij}(r_{ij}), \tag{1}$$

with

$$\rho_i = \sum_{j\neq i} f_i(r_{ij}) \tag{2}$$

Where ϕ_{ij} is a pair wise term between atoms i and j separated by a distance r_{ij}, and F_i is the embedding energy term associated with the local electron density ρ_i calculated from the electron density $f_i(r_{ij})$ at the site i arising from atom j. On the other hand, to describe the atomic interactions for Fe-based systems, including Fe-Ni, Fe-Ni-Co, Fe-Ni-Cr, and the medium-entropy alloy (MEA) Fe-Ni-Cr-Mn, we adopted the modified embedded-atom method (MEAM) potential parametrized by Choi *et al.* [53], which was successfully applied to reproduce fundamental structural properties of the CoCrFeMnNi HEA and shown to be suitable for the design of new complex alloys.The Fe-Cu-Ni systems were modeled using an EAM alloy potential including short-range ZBL corrections [54]. The Sm-Al systems were described using the EAM potential developed for Al-Sm alloys [55], while $Cu_{65}Zr_{35}$ metallic glasses were modeled using both a conventional EAM potential [56] and a machine-learning potential based on the atomic cluster expansion (ACE) formalism [57] in order to provide a more accurate description of the local structural order.

For each sample, we prepared a cubic simulation box with side lengths of 100 Å (i.e., 100 × 100 × 100 Å^3), containing around 55,296 atoms, with periodic boundary conditions in all three dimensions. The Newtonian equations of motion were solved using the velocity-Verlet algorithm with a time step of 1 fs. The temperature and pressure of the system were controlled via the Nose-Hoover thermostat and barostat [58]. All systems underwent a gradual heating process within the isothermal-isobaric (NPT) ensemble at a constant pressure of 0 GPa. The systems were heated up from 300 K to 2500 K, at a rate of 5×10^{12} K/s, ensuring complete melting. The system was then relaxed in the canonical (NVT) ensemble for 100 ps in the liquid state. Finally, rapid cooling was performed back to 300 K under the NPT ensemble, at a rate of 10^{13} K/s. This rapid cooling prevented atomic reorganization into a crystalline structure, thereby maintaining the glassy configuration of the MGs. The obtained MGs were first relaxed under NPT conditions for 100 ps to eliminate residual stresses and ensure structural equilibrium at zero pressure. Subsequently, the systems were heated to the desired temperature at a rate of 5×10^{12} K/s under the NPT ensemble. Additional heating rates were tested to verify the robustness of the observed trends and are reported in the Supplementary Material Fig. S1 [59]. The

selection of the optimal heating rate is also supported by prior work indicating that rates below a certain threshold can lead to partial crystallization, while higher rates produce consistent thermal expansion behavior [60]. The effect of intermediate NPT relaxations during heating is discussed in the Supplementary Material Fig. S2 [59]. No significant difference in thermal expansion behavior was observed, and the direct heating protocol was adopted for computational efficiency. The analysis and visualization were conducted using OVITO (Open Visualization Tool) software [61].

A. Radial distribution function

The radial distribution function (RDF) is one of the most important metrics for characterizing the structural properties of complex materials. It describes the probability of finding a neighboring atom at a distance r from a central atom and can be calculated using the following expression [62]:

$$g(r) = \frac{1}{4\pi r^2 \rho_j}\left[\frac{dN_{ij}(r)}{dr}\right] \tag{3}$$

where i, j are atoms and $N_{ij}(r)$ stands for the average number of j atoms in the sphere centered on i atoms with a radius r.

B. Voronoi analysis and motif classification

Voronoi polyhedra (VPs) are categorized into three types. Icosahedral-like polyhedra are defined as those with $n_5 \geq 8$, consistent with previously established criteria [63]. Crystal-like polyhedra correspond to a set of 24 Voronoi indices derived from thermally perturbed FCC, BCC, and HCP reference structures. Mixed-like polyhedra comprise all remaining configurations. To mitigate the well-known sensitivity of Voronoi tessellation to thermal vibrations, quasi-degenerate faces were filtered using an area threshold identified from the local minimum of the face-area distribution (see Supplementary Material, Fig. S5). For multicomponent alloys, radical Voronoi tessellation was employed, using the following atomic radii: Fe (1.26 Å), Ni (1.24 Å), Co (1.25 Å), Cr (1.28 Å), Mn (1.27 Å), Al (1.43 Å), Cu (1.28 Å), Zr (1.60 Å), and Sm (1.85 Å). Further details on the classification criteria are provided in the Supplementary Material [59].

III. RESULTS

A. Structural Formation and Evolution of MGs

Figure 1 presents the variation of the $g(r)$ function during the rapid quenching process for the following materials: $Ni_{75}Al_{25}$, $Ni_{70}Al_{20}Co_{10}$, $Fe_{60}Ni_{30}Co_{10}$ and $Fe_{50}Ni_{20}Co_{10}Cr_{10}Mn_{10}$. At high temperature, $g(r)$ exhibits a sharp first peak, followed by rapidly decaying oscillations. This behavior is characteristic of the liquid state, where the absence of long-range atomic correlations signifies a lack of long-range order. Upon cooling, $g(r)$ shows a pronounced sharpening of the first peak, indicating an enhancement of the short-range order (SRO). Concurrently, the second peak splits into two distinct sub-peaks, a signature of the development of medium-range order (MRO) and increased cluster connectivity. This trend, consistent across all studied compositions (see Fig. S3 in the Supplementary material [59]), marks the transition from the liquid to the supercooled state. Such structural signatures align with other metallic glass systems, including Cu_xZr_{100-x} [64], $Zr_{50}Cu_{50-x}Al_x$ [65], ZrCo [20], and $TiAl_3$ [66], confirming that the used cooling rate successfully produced glass structures for all systems.

Figure. 2 shows the system volume as a function of temperature during the heating and cooling processes for $Ni_{75}Al_{25}$, $Ni_{70}Al_{30}Co_{20}$, $Fe_{60}Ni_{30}Co_{10}$ and $Fe_{50}Ni_{20}Co_{10}Cr_{10}Mn_{10}$. During the heating process, the volume increases almost linearly with temperature until a sudden jump occurs (T_m=1917 K for $Ni_{75}Al_{25}$, T_m=1986 K for $Ni_{70}Al_{30}Co_{20}$, T_m=2143 K for $Fe_{60}Ni_{30}Co_{10}$, and T_m=2061 K for $Fe_{50}Ni_{20}Co_{10}Cr_{10}Mn_{10}$), indicating the onset of melting. Conversely, during cooling, the volume decreases continuously, with a change in slope at the glass transition temperature (T_g). The intersection between the two linear adjustments, applied respectively to the glassy and liquid regions of the curve $V(T)$, determines the glass transition temperature, which is found to be T_g≈1112 K for $Ni_{75}Al_{25}$, T_g≈1038 K for $Ni_{70}Al_{30}Co_{20}$, T_g≈1075 K for $Fe_{60}Ni_{30}Co_{10}$, and T_g≈1028 K for $Fe_{50}Ni_{20}Co_{10}Cr_{10}Mn_{10}$. However, after solidification, the excess volume between the beginning of heating and the end of quenching is referred to as free volume [67], suggesting that the alloy lacks a crystalline structure and has transitioned into an amorphous state. The same behavior was observed for the other MGs studied (see Fig. S4 in the Supplementary material [59]). This observation is consistent with findings from various studies, which concluded that the material has indeed reached a glassy state, with the crystalline phase being inhibited [68, 69].

B. Investigation of thermal expansion in MGs

1. *Global thermal expansion*

To quantify the thermal expansion behavior of the MGs, the volumetric strain $(V - V_0)/V_0$ was plotted as a function of temperature during the heating stage (Fig. 3). The volumetric coefficient of thermal expansion (β) was extracted from linear fits of the volumetric strain in specific temperature ranges corresponding to the glassy and liquid states. For all studied MG systems,

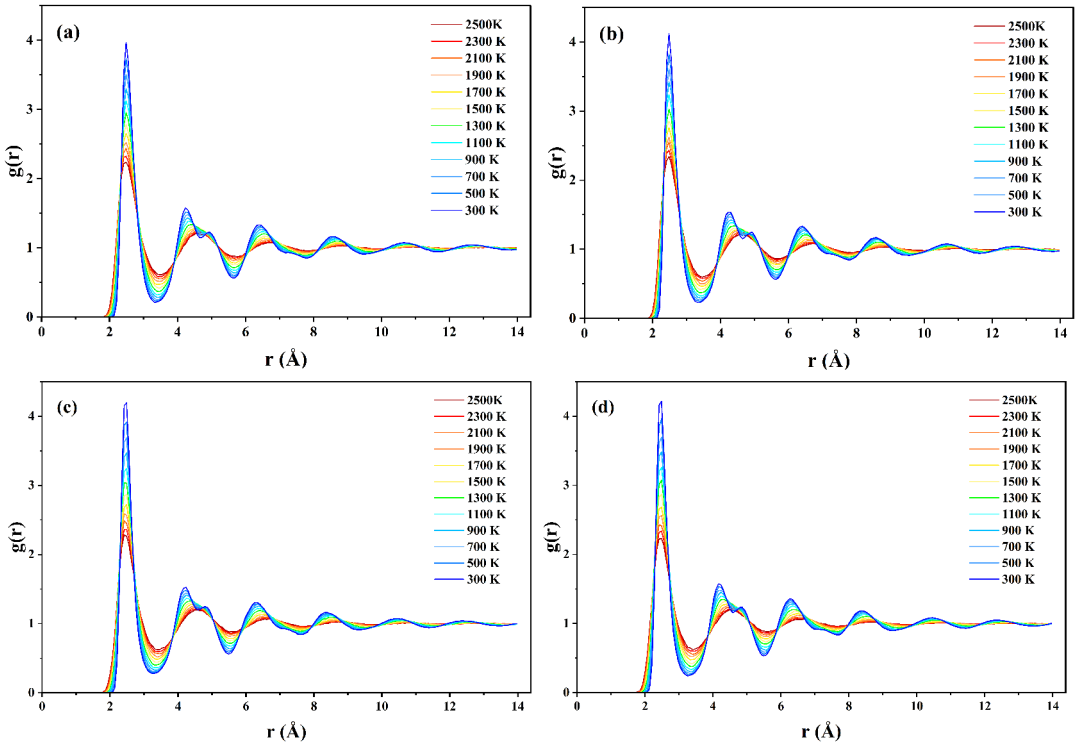

FIG. 1. Evolution of the radial distribution function $g(r)$ during the cooling process for the four investigated metallic glass systems: (a) $Fe_{50}Ni_{20}Co_{10}Cr_{10}Mn_{10}$, (b) $Fe_{60}Ni_{30}Co_{10}$, (c) $Ni_{70}Al_{20}Co_{10}$, and (d) $Ni_{75}Al_{25}$.

the glassy-state CTE was determined in the temperature range from 300 to 900 K, while the liquid-state CTE was obtained between 1300 and 2000 K. An exception is made for the monoatomic Al MG, where the fitting ranges were 300–600 K for the glassy state and 700–1400 K for the liquid state, due to its lower characteristic transition temperatures.

The analysis of volumetric strain as a function of temperature provides key insights into the thermal expansion behavior of the studied systems. In the low-temperature regime, MGs exhibit a linear increase in volume, consistent with positive thermal expansion. The onset of the glass transition temperature (T_g) is marked by a clear change in slope, signifying the structural shift from a glassy to a supercooled liquid state. Above T_g, the slope becomes significantly steeper, indicating that the volumetric expansion coefficient (β) is higher in the liquid state than in the glassy state. This behavior, widely documented in both theoretical and experimental literature [70–73], reflects the fundamental structural rearrangement and the increased atomic mobility that characterize the liquid regime.

In both crystalline and amorphous materials, thermal expansion is mainly governed by the anharmonic nature of interatomic interactions, which is the primary origin of thermal expansion of both glasses and crystals. In liquids, however, the absence of long-range order allows translational atomic motions and structural rearrangements associated with viscous flow, which introduce an additional configurational contribution. As a result, the volumetric thermal expansion coefficient of liquids β_L, can be considered the combined effect of a vibrational component comparable to that observed in glasses and crystals and a configurational component specific to the liquid state [26, 74, 75]. Consequently, thermal expansion is lower in the glassy state and significantly higher in liquids and supercooled liquids, owing to the additional configurational contribution. The variation of volume with temperature was extracted by fitting the obtained curves with a linear function, and the volumetric thermal expansion coefficients (β) for the MGs in both the solid and liquid states were determined from the following macroscopic equation [76]:

$$\frac{V - V_0}{V_0} = \beta \Delta T = \beta (T - T_0) \tag{4}$$

where V_0 is the initial volume at temperature T_0, V is the volume at temperature T, and β is the volumetric coefficient of thermal expansion.

Table I summarizes the volumetric thermal expansion coefficients of the studied MGs in both the glassy (β_G) and supercooled liquid (β_L) states. A considerable increase in the thermal expansion coefficient is observed during the transition from the glassy to the liquid state

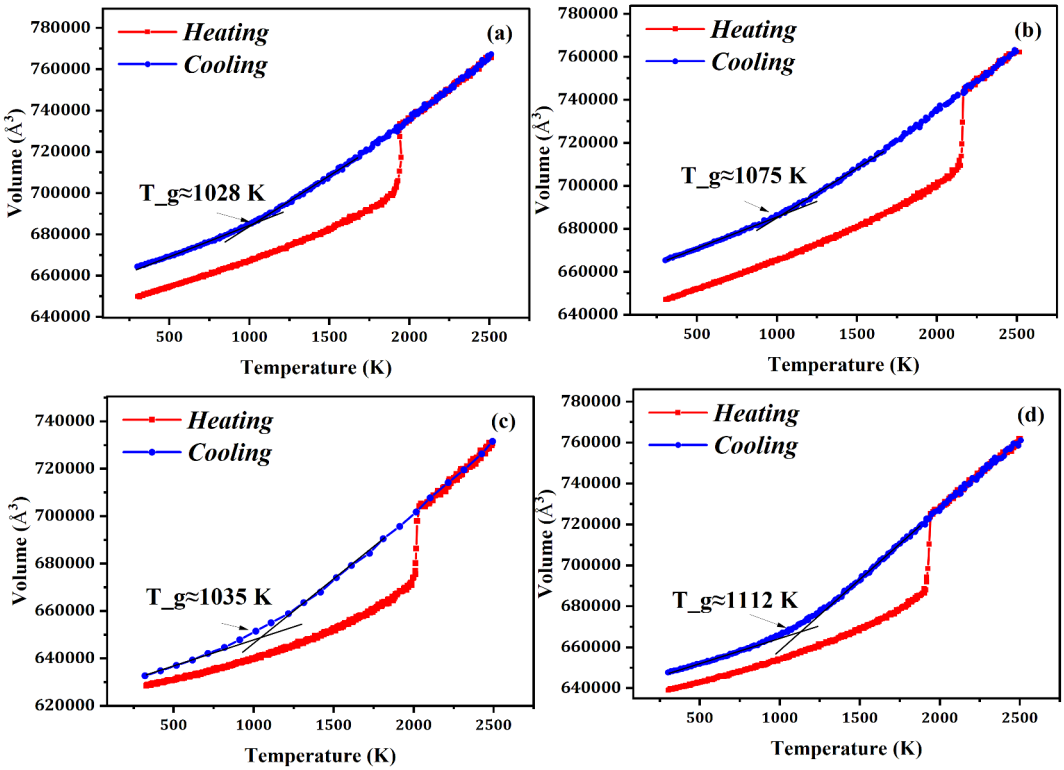

FIG. 2. Volume as a function of temperature during heating (red curves) and cooling (blue curves) for the four studied metallic glass systems. Melting is indicated by the abrupt change in the heating curves, while the glass transition temperature T_g is identified from the intersection of linear fits to the low- and high-temperature regimes: (a) $Fe_{50}Ni_{20}Co_{10}Cr_{10}Mn_{10}$, (b) $Fe_{60}Ni_{30}Co_{10}$, (c) $Ni_{70}Al_{20}Co_{10}$, and (d) $Ni_{75}Al_{25}$.

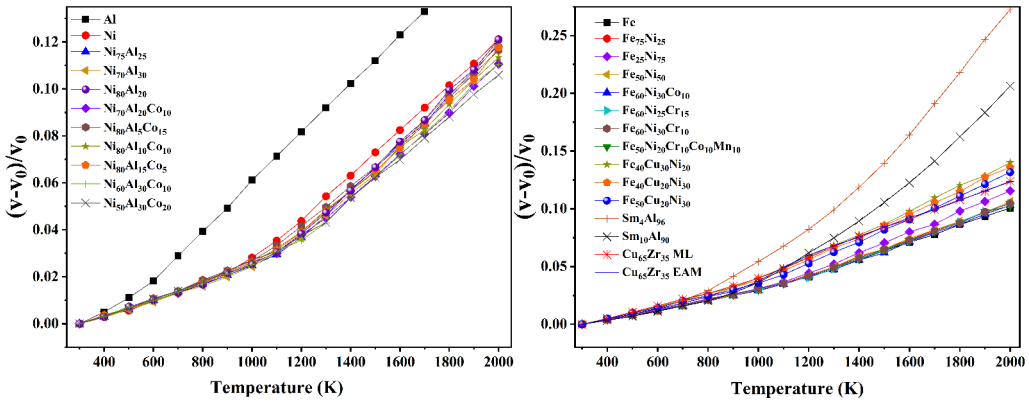

FIG. 3. Temperature dependence of volumetric strain in all studied systems. Low-temperature curves are used to extract thermal expansion coefficients of MGs, while high-temperature curves are used for liquids.

in all systems studied. The coefficient of the liquid state (β_L) is always higher than that of the glassy state (β_G), reflecting a transition toward a more disordered structural state. This increase has been attributed to the larger free volume in the supercooled and equilibrium liquid phases, accompanied by the enhanced atomic mobility inherent to the liquid state [75].

In the glassy state, Al-based metallic glass exhibits the highest thermal expansion coefficient among the studied systems. In contrast, Ni-based glasses (Ni, $Ni_{75}Al_{25}$, and $Ni_{70}Al_{20}Co_{10}$) exhibit considerably lower values, suggesting higher dimensional stability at low temperature. In comparison, Fe-based glasses ($Fe_{75}N_{25}$, $Fe_{60}Ni_{30}Co_{10}$ and $Fe_{50}Ni_{20}Co_{10}Cr_{10}Mn_{10}$) show higher β_G values than Ni-based glasses. However, this trend is reversed in the liquid state: Fe-based alloys exhibit lower thermal ex-

TABLE I. Thermal expansion coefficients β_v and glass transition temperature T_g of MGs in the glassy and liquid states.

Composition	Glass β_G (10^{-5} K^{-1})	Liquid β_L (10^{-5} K^{-1})	β_L/β_G	T_g (K)
Al	6.07 ± 0.34	10.50 ± 0.13	1.72	602.04
Ni	3.68 ± 0.24	9.54 ± 0.05	2.59	1050.01
Fe	4.20 ± 0.09	7.51 ± 0.06	1.78	1102.78
$Fe_{75}Ni_{25}$	4.36 ± 0.10	7.85 ± 0.06	1.80	1100.86
$Fe_{50}Ni_{50}$	4.16 ± 0.04	7.91 ± 0.12	1.90	1054.08
$Fe_{25}Ni_{75}$	4.35 ± 0.05	8.98 ± 0.13	2.06	1087.11
$Fe_{50}Cu_{20}Ni_{30}$	5.00 ± 0.06	9.92 ± 0.10	1.98	1025.80
$Fe_{40}Cu_{40}Ni_{20}$	5.42 ± 0.06	10.42 ± 0.10	1.92	1024.74
$Fe_{40}Cu_{30}Ni_{30}$	5.22 ± 0.08	10.18 ± 0.10	1.95	1019.40
$Fe_{60}Ni_{25}Cr_{15}$	4.32 ± 0.05	8.10 ± 0.07	1.88	1096.36
$Fe_{60}Ni_{30}Cr_{10}$	4.31 ± 0.05	7.91 ± 0.08	1.83	1101.49
$Fe_{60}Ni_{30}Co_{10}$	4.12 ± 0.06	7.98 ± 0.10	1.94	1090.00
$Fe_{50}Ni_{30}Co_{10}Cr_{10}Mn_{10}$	4.30 ± 0.03	7.86 ± 0.14	1.83	1095.67
$Ni_{70}Al_{30}$	3.34 ± 0.06	10.58 ± 0.23	3.17	1076.91
$Ni_{75}Al_{25}$	3.44 ± 0.05	10.30 ± 0.15	2.99	1065.78
$Ni_{80}Al_{20}$	3.51 ± 0.11	10.48 ± 0.16	2.99	1068.34
$Ni_{70}Al_{20}Co_{10}$	3.63 ± 0.13	9.35 ± 0.13	2.58	1096.90
$Ni_{80}Al_5Co_{15}$	3.75 ± 0.08	9.57 ± 0.20	2.55	1077.06
$Ni_{80}Al_{10}Co_{10}$	3.70 ± 0.14	9.33 ± 0.18	2.52	1078.78
$Ni_{80}Al_{15}Co_5$	3.55 ± 0.12	9.83 ± 0.22	2.77	1086.93
$Ni_{60}Al_{30}Co_{10}$	3.49 ± 0.06	9.65 ± 0.10	2.77	1080.41
$Ni_{50}Al_{30}Co_{20}$	3.70 ± 0.09	8.87 ± 0.10	2.40	1084.64
$Ni_{80}Co_{20}$	3.87 ± 0.11	9.51 ± 0.30	2.46	1076.91
Sm_4Al_{96}	6.15 ± 0.48	23.27 ± 0.20	3.78	923.60
$Sm_{10}Al_{90}$	4.43 ± 0.21	18.81 ± 0.57	4.25	956.09
$Cu_{65}Zr_{35}$ ML	5.40 ± 0.05	8.01 ± 0.10	1.48	994.88
$Cu_{65}Zr_{35}$ EAM	4.78 ± 0.07	7.90 ± 0.06	1.65	1008.69

pansion compared to Ni-based ones, reflecting a stronger resistance to thermal expansion upon heating above T_g. These findings are consistent with the results reported by Komatsu *et al.* in $(Fe_xNi_{1-x})_{78}Si_8B_{14}$ MGs [77], where the thermal expansion coefficient of as-quenched samples decreased monotonically with increasing Fe content. This behavior was attributed to the magnetic contribution to the thermal expansion coefficient in Fe-rich alloys, where large volume magnetostriction partially compensates the normal lattice expansion, leading to an Invar-like reduction of thermal expansion that is particularly pronounced in $Fe_{78}Si_8B_{14}$ [77].

The glass transition temperature also varies across compositions, confirming distinct thermal behaviors among the studied alloys [78]. Although no direct correlation between β and T_g was found in our study, previous works have suggested that the fragility parameter (m) may provide the missing link between thermal expansion and glass transition dynamics, as fragile glasses tend to exhibit larger expansion coefficients at lower T_g [75–80].

2. *Local thermal expansion from Voronoi analysis*

Macroscopic thermal expansion coefficients represent averaged quantities and therefore mask the intrinsic structural heterogeneity of MGs. To identify the atomic-scale origins of thermal expansion, a local analysis based on distinct atomic motifs is required. In the following, local thermal expansion coefficients are evaluated by monitoring the temperature-dependent atomic volumes of individual Voronoi polyhedra, enabling direct comparison across different local atomic motifs. Fig. 4 presents the spatial distribution of local atomic volume fluctuations ($(V - V_0)/V_0$) at 400 K and 2000 K, illustrating how atomic volumes are distributed within the system at different temperatures. These snapshots clearly show that thermal expansion is highly heterogeneous at the atomic scale, with some regions expanding much more strongly than others upon heating. This observation is consistent with the findings of Shang *et al.* [30], who reported that MGs exhibit heterogeneous thermal expansion coefficients, analogous to the heterogeneity observed in their elastic constants. They further showed that such non-uniform expansion can generate internal stresses strong enough to trigger local atomic rearrangements, a mechanism proposed to explain cryogenic rejuvenation during thermal cycling, although resolving this mechanism directly in MD simulations remains difficult [30]. To clarify how these local responses contribute to the macroscopic thermal behavior, we next analyze the role of different types of local clusters in thermal expansion and thermal stability.

To study the evolution of different local atomic structures during the heating process, we used the Voronoi tessellation analysis (VTA) method, which characterizes each atom by four integer indices called Voronoi indices $\langle n_3, n_4, n_5, n_6 \rangle$, with n_i denoting the number of faces of

the Voronoi polyhedron with i edges. For example, the full icosahedral cluster is represented by the Voronoi index $\langle 0,0,12,0\rangle$ [63, 81, 82]. Voronoi polyhedra (VPs) are generally categorized into three types: icosahedral-like, mixed-like, and crystal-like. Further details on the classification criteria and representative Voronoi indices are provided in the Supplementary Material [59] (Section 1: Voronoi tessellation analysis and Section 2: Classification of Voronoi Polyhedra).

Fig. 5 displays the variation of the main VP families as function of temperature evolution, for $Ni_{70}Al_{20}Co_{10}$, $Fe_{60}Ni_{30}Co_{10}$ and $Fe_{50}Ni_{20}Co_{10}Cr_{10}Mn_{10}$. At low temperatures, icosahedral-like polyhedra dominate the glassy state. As temperature increases, their fraction progressively decreases while mixed-like polyhedra steadily increase and become predominant after the glass transition. The fraction of crystal-like polyhedra remains low (around 5%) over the entire temperature range, indicating the absence of crystallization. Similar behavior is observed for all systems (Supplementary material Fig. S6 [59]), demonstrating a temperature-induced transformation from icosahedral-like to mixed-like local structures.

To extract the contribution of each substructure to the thermal expansion, we calculated the average atomic volume for each Voronoi polyhedra at each temperature during heating. Note that the polyhedra at a given temperature are not necessarily the same at other temperatures, as atomic motion continuously reshapes local environments, making it challenging to track the expansion of individual polyhedra. Instead, we consider the average atomic volume of all polyhedra of the same type at each temperature. This allows us to quantify the local volumetric thermal expansion for each class of polyhedra and compare it with the global volumetric thermal expansion. For each type, the average atomic volume at a temperature T was compared to its value at $T = 300$ K. The resulting relative change defines the local volumetric strain. In contrast, the relative change in the total system volume represents the global volumetric strain, allowing a direct comparison between local and global expansion coefficients.

Fig. 6 presents the temperature dependence of the local and global volumetric strains in $Ni_{70}Al_{20}Co_{10}$, $Fe_{60}Ni_{30}Co_{10}$, and $Fe_{50}Ni_{20}Co_{10}Cr_{10}Mn_{10}$. The figures reveal diverse thermal responses of Voronoi polyhedra across the glassy and liquid states, highlighting the complexity of atomic-level thermal behavior. Below the glass transition, the average atomic volumes of most Voronoi polyhedra increase linearly with temperature, in parallel with the overall volume expansion of the MGs. Above the glass transition, however, this trend changes, indicating a shift in the local structural response to heating.

The local thermal expansion coefficient for each type of Voronoi polyhedra is quantified by fitting the curves in Fig. 6 with a linear function using Eq. (5) in both the glassy and liquid states:

$$\frac{< v > - < v_0 >}{< v_0 >} = \beta(T - T_0) \tag{5}$$

Here, $\langle v_0\rangle$ and $\langle v\rangle$ denote the average atomic volume of a given Voronoi polyhedron type at temperatures T_0 and T, respectively, and β is the corresponding local thermal expansion coefficient.

By comparing local and global coefficients of thermal expansion (β_G and β_L) in the glassy and liquid states (Table II), we can identify which Voronoi polyhedra contribute most to the overall thermal expansion. Analysis of the relative volume variation $((\langle v\rangle - \langle v_0\rangle)/\langle v_0\rangle)$, before and after the glass transition, provides insights into the structural origins of thermal expansion. In both the glassy and liquid states, the CTE of Mixed-like polyhedra closely matches that of the overall system. For instance, in the MEA system (Fig. 6 and Table II), the CTE of mixed polyhedra in the glassy state is 4.44×10^{-5} K^{-1}, compared to 4.30×10^{-5} K^{-1} for the overall system, and 7.48×10^{-5} K^{-1} in the liquid state close to the system value of 7.86×10^{-5} K^{-1}. This demonstrates that mixed polyhedra dominate the overall thermal expansion behavior. In contrast, icosahedral polyhedra consistently exhibit lower CTE values, and crystal-like polyhedra show relatively higher CTE values. This behavior of the crystal-like polyhedra can be attributed to their low fraction in the system: their contribution to the macroscopic response remains limited despite their comparatively larger local volume fluctuations. A similar behavior is observed in other systems we studied, as shown in the Supplementary Material Fig. S7 and Table S1 [59].

To further support the analysis of local thermal expansion based on atomic volumes, we examined the temperature dependence of the potential energy of different polyhedron types. Fig. 7 shows the evolution of the average atomic potential energy of the global system and of the icosahedral-like and mixed-like Voronoi polyhedra during heating. For all alloys, the potential energy increases with temperature, but there are clear differences between the structural families. Icosahedral polyhedra consistently exhibit the lowest potential energy, consistent with previous studies showing that icosahedral order corresponds to an energetically stable local configuration in MGs [83–85]. In contrast, mixed-like polyhedra have the highest potential energy, which increases more rapidly with temperature, reflecting their greater sensitivity to thermal fluctuations. The global system energy lies between these two curves, indicating the averaged contribution of all local environments. A similar behavior is observed in other systems we studied, as shown in the Supplementary Material Fig. S8 [59].

Crystal-like polyhedra are not shown in Fig. 7 because their very low population throughout the heating process leads to considerable statistical noise in the average potential energy. Furthermore, since crystal-like atoms are surrounded predominantly by icosahedral-like and

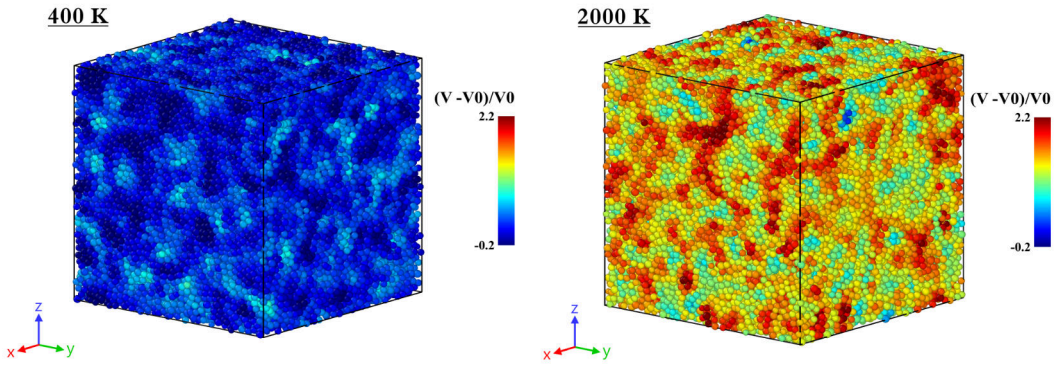

FIG. 4. Spatial distribution of local atomic volume fluctuations $(V-V_0)/V_0$ at 400 K and 2000 K, highlighting the heterogeneous nature of thermal expansion.

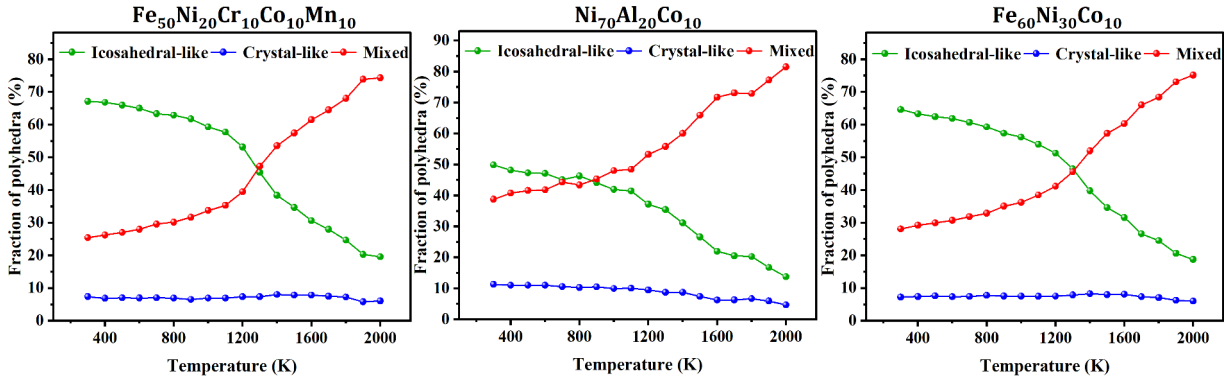

FIG. 5. Variation of Icosahedral-like, Crystal-like, and Mixed-like Voronoi polyhedra with temperature in MGs.

mixed-like neighbors, their potential energy reflects the local chemical environment rather than an intrinsic property of crystal-like configurations. Including these data without this context would risk misinterpretation.

3. *Local thermal expansion from $G(r)$*

The local thermal expansion can also be evaluated from the temperature-dependent shift of the first peak of the pair distribution function, $G(r)$. As temperature increases, the peak position reflects changes in the average nearest-neighbor distance, providing a measure of atomic-scale expansion. This approach complements the Voronoi-based analysis by linking structural rearrangements to thermal expansion at the short-range order level. In several recent studies [38, 42, 86, 87], the position of the maximum of the first peak in $g(r)$ was used to determine the local coefficient of thermal expansion (CTE). These studies reported apparent bond contraction, since the peak shifts toward smaller r values with increasing temperature. However, this apparent contraction is an artifact that does not represent the true thermal behavior of the average bond length. Gangopadhyay *et al.* [87] attributed this apparent negative thermal expansion in the liquid state to the influence of pair partial atom contributions on the peak intensity of $g(r)$. Similarly, Lou *et al.* [88] and Su *et al.* [38] linked negative CTEs in liquids to the transformation of highly-coordinated clusters into lower-coordinated ones. It should be noted that $g(r)$ is normalized with respect to the average density, describing only the relative probability of finding an atom at a distance r from a reference atom. As such, it does not directly yield the true average bond length. Moreover, previous studies neglected the effect of peak asymmetry, focusing only on the position of the first peak's maximum. For completeness, the local thermal expansion was also estimated using the conventional method based on the position of the first peak of $g(r)$, leading to an apparent negative expansion in the liquid state, in agreement with previous reports. These results are provided in the Supplementary material Fig. S9 [59].

To overcome the limitations of the radial distribution function $g(r)$, we analyzed the radial probability distribution function $G(r)$, defined as $G(r) = 4\pi r^2 \rho g(r)$, during the heating process (Fig. 8). Unlike $g(r)$, which describes relative atomic correlations, $G(r)$ represents a probability density function, allowing the direct calculation of physically meaningful quantities, such as coordination

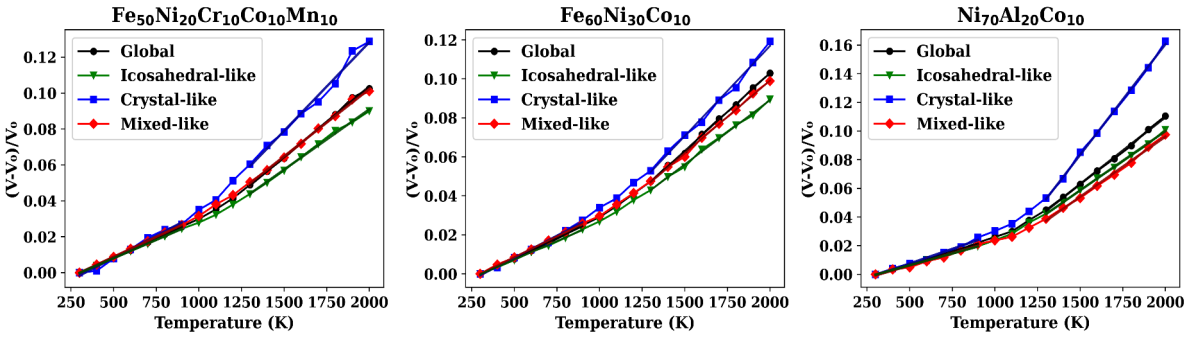

FIG. 6. Variation of global volume and atomic volume of icosahedral-like, crystal-like, and mixed-like Voronoi polyhedra During Heating.

TABLE II. Comparison between global and local volumetric thermal expansion coefficients in the glassy (β_G) and liquid (β_L) states for different Voronoi polyhedron types in selected MGs. The rest of the samples are shown in Tab. S4-S8 in the SM [59].

System / Polyhedra	Glass β_G (10^{-5} K^{-1})	Liquid β_L (10^{-5} K^{-1})	β_L/β_G
$Fe_{50}Ni_{20}Co_{10}Cr_{10}Mn_{10}$			
Global	4.30 ± 0.0283	7.86 ± 0.135	1.86
Crystal-like	4.93 ± 0.28	9.87 ± 0.46	2.00
Mixed-like	4.44 ± 0.023	7.48 ± 0.154	1.68
Icosahedral-like	4.09 ± 0.023	6.72 ± 0.139	1.64
$Fe_{60}Ni_{30}Co_{10}$			
Global	4.12 ± 0.06	7.98 ± 0.10	1.93
Crystal-like	4.57 ± 0.15	9.24 ± 0.29	2.02
Mixed-like	4.26 ± 0.05	7.46 ± 0.13	1.75
Icosahedral-like	3.80 ± 0.06	6.60 ± 0.13	1.73
$Ni_{70}Al_{20}Co_{10}$			
Global	3.63 ± 0.13	9.35 ± 0.15	2.57
Crystal-like	4.09 ± 0.24	15.3 ± 0.24	3.74
Mixed-like	3.45 ± 0.20	8.45 ± 0.12	2.44
Icosahedral-like	3.26 ± 0.80	8.26 ± 0.11	2.53

numbers, through its integrals. Fig. 8 shows $G(r)$ for the $Ni_{70}Al_{20}Co_{10}$ alloy across the glassy, supercooled liquid, and equilibrium liquid states over the temperature range 300–2000 K. The first peak of $G(r)$ is particularly relevant for investigating local thermal expansion, as it reflects the short-range atomic order that governs the structural stability of MGs. As shown in Fig. 8, this peak exhibits a noticeable asymmetry. Following Sukhomlinov and Müser [86], the first peak of $G(r)$ was fitted using a skewed normal distribution (SND). Rather than tracking the mode (peak position), we tracked the mean of the fitted distribution, which corresponds to the average bond length. Here we apply this approach to characterize the local thermal expansion of MGs across a broad compositional space, complementing the Voronoi-based motif analysis.

The relative shift of the mean bond length was quantified as $\frac{\langle r\rangle - \langle r_0\rangle}{\langle r_0\rangle}$, as shown in Fig. 9.

The results indicate that the mean interatomic distance associated with the first peak of $G(r)$ increases with temperature in all studied systems with a noticeable change in slope around the glass transition temperature (T_g), reflecting the structural transformation from the amorphous solid to the liquid state. This trend is consistent with the local thermal expansion evaluated from atomic volume changes, which also indicates positive expansion. In contrast to previous studies reporting apparent contraction from the first peak of $g(r)$, our approach demonstrates true thermal expansion. Similar behavior is observed in other metallic glass systems (Supplementary material, Fig. S10 [59]), confirming that the trends are not system-specific but rather general.

IV. DISCUSSION

All analyses carried out in this work, including macroscopic volume expansion, changes in local atomic environments, the potential energy of Voronoi motifs, and bond-length evolution, provide a coherent understanding of the structural origin of thermal expansion in MGs.

At the macroscopic scale, all the studied alloys exhibit positive thermal expansion, with a pronounced change in slope near the glass transition temperature. This change

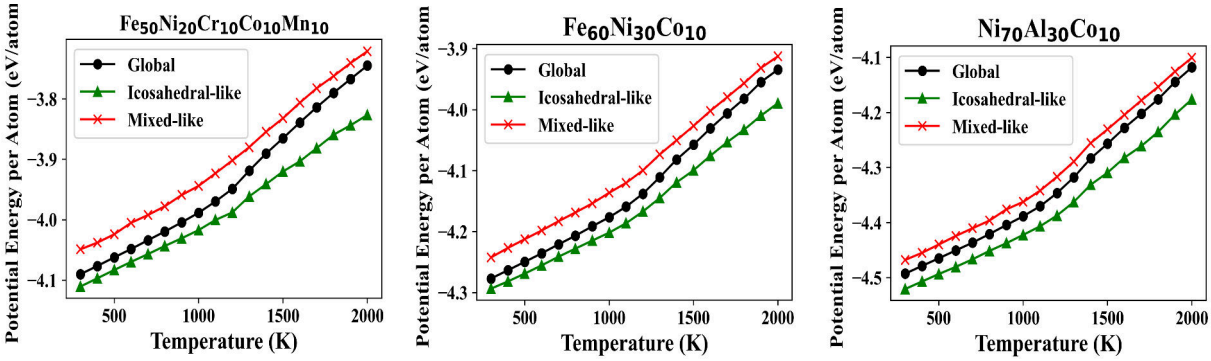

FIG. 7. Average atomic potential energy of the global system and of icosahedral-like, and mixed-like Voronoi polyhedra as a function of temperature.

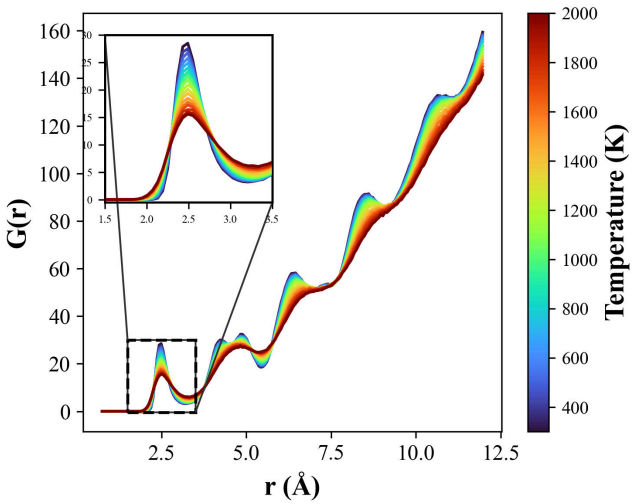

FIG. 8. Radial probability distribution function $G(r)$ of $Ni_{70}Al_{20}Co_{10}$ metallic glass at different temperatures. The inset highlights the evolution of the first peak.

reflects the transition from a purely vibrational thermal response in the glassy state to a regime where additional configurational contributions become active in the supercooled liquid state. In MGs, the thermal expansion below T_g is mainly governed by vibrational contributions arising from the anharmonicity of interatomic potentials, leading to a linear volume–temperature relationship with a relatively low thermal expansion coefficient. Above T_g, the volume continues to evolve linearly with temperature, but with a significantly higher slope. This increase in the thermal expansion coefficient is associated with the activation of additional configurational contributions enabled by enhanced atomic mobility and structural relaxation in the supercooled liquid state, as discussed by Lunkenheimer [74], and in earlier studies [75, 89].

The glass transition temperature varies slightly with composition among the investigated alloys. Previous experimental and theoretical studies have reported an inverse correlation between the thermal expansion coefficient and the glass transition temperature, and have further suggested that this apparent relationship is mediated by the fragility of the supercooled liquid, with more fragile systems generally exhibiting higher thermal expansion coefficients and lower T_g values, as discussed for instance by Gangopadhyay *et al.* [90], Lunkenheimer *et al.* [74] and Guo *et al.* [91]. A negative trend is observed between the liquid thermal expansion coefficient β_L and the glass transition temperature T_g across the investigated systems (See Fig. 10). This trend is presented as physically consistent with prior literature rather than as a predictive quantitative relation: metallic glasses with lower liquid thermal expansion tend to exhibit higher glass transition temperatures, as reported by Gangopadhyay *et al.* [90], Lunkenheimer *et al.* [74], and Guo *et al.* [91].

The macroscopic response masks the strong heterogeneity inherent to MGs. As illustrated in Fig. 4, some atomic regions expand much more than others, revealing pronounced spatial variations in local thermal expansion, in agreement with the observations of Shang *et al.* [30]. They showed that such non-uniform expansion generates internal stresses capable of inducing local atomic rearrangements, a mechanism proposed to explain cryogenic rejuvenation during thermal cycling. However, Shang *et al.* did not fully address the nature of these expanding regions, nor did they specify which types of atomic environments are more susceptible to expansion and which remain more stable during heating. Furthermore, although overall expansion is homogeneous on a macroscopic scale, local contributions to thermal expansion can vary considerably depending on atomic structures.

Understanding the structural origin of this heterogeneity, therefore, requires analyzing the thermal response of different atomic environments. To this end, we examined the evolution of different Voronoi polyhedra during heating. As shown in Fig. 5, the population of icosahedral-like polyhedra gradually decreases during heating, while that of mixed-like polyhedra increases significantly. This evolution highlights a topological transition from densely packed icosahedral-like configurations to more disordered

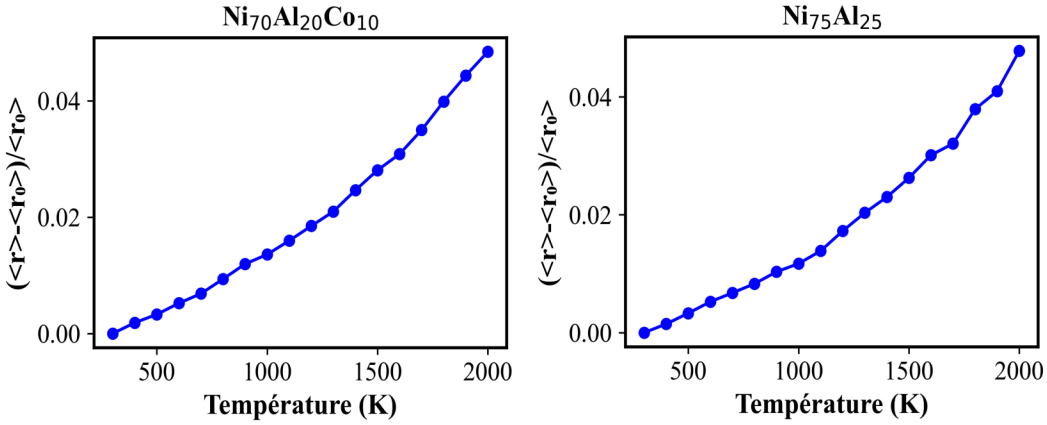

FIG. 9. Relative change of the mean nearest-neighbor distance with temperature for $Ni_{70}Al_{20}Co_{10}$ and $Ni_{75}Al_{25}$ MGs.

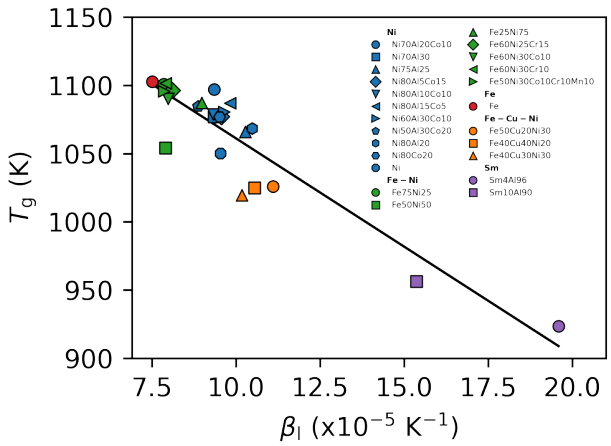

FIG. 10. Liquid thermal expansion coefficients β_L plotted as a function of the corresponding glass transition temperature T_g for the investigated metallic glasses. The solid line represents a linear fit, showing a negative trend. The main purpose of the fitted line is to highlight the trend and not a general correlation.

mixed-like environments, consistent with previous structural observations [92–95]. In contrast, crystal-like polyhedra remain at very low fractions, limiting their contribution to the macroscopic response.

Local thermal expansion analysis based on atomic volume variations (Fig. 6) further reveals distinct responses depending on polyhedron type. Icosahedral polyhedra exhibit the smallest volume variations, reflecting their compact geometry and resistance to thermal deformation. This stabilizing behavior is consistent with their low potential energy (Fig. 7) and with previous studies identifying icosahedral clusters as an energetically favorable local configuration in MGs [83–85]. In contrast, mixed-like polyhedra exhibit local expansion values close to those of the overall system in both the glassy and liquid states, indicating that they dominate the macroscopic thermal expansion. This behavior can be attributed to their more flexible atomic environments, higher potential energy, and enhanced anharmonicity, as supported by the energetic analysis (Fig. 7). Although crystal-like polyhedra exhibit greater local expansion, their very low population makes their contribution negligible. These combined structural and thermal features provide a coherent picture of the macroscopic thermal expansion of MGs. The convergence of volumetric and energy analyses demonstrates that thermal expansion is primarily governed by mixed-like polyhedra, while icosahedral polyhedra are consistently associated with lower local expansion across all investigated systems. The enhanced packing efficiency and geometric regularity of icosahedral units reduce the anharmonicity of the local potential energy landscape, providing a structural basis for the observed behavior consistent with previous studies [83–85]. This motif-dependent ordering of local CTEs, $\beta_{\mathrm{ico}} < \beta_{\mathrm{mixed}} < \beta_{\mathrm{crystal}}$, is preserved across 25 compositions spanning five chemical families, multiple interatomic potentials including a machine-learning potential of near-DFT accuracy, and cooling rates spanning nearly two orders of magnitude (See Tab. S2 and S3). This robustness suggests that the motif-dependent thermal response is a general characteristic of MGs rather than an artifact of simulation conditions.

Although cooling rates employed in MD simulations remain orders of magnitude higher than those achievable experimentally for metallic alloys, the motif-resolved CTEs show only marginal sensitivity to the cooling rate within the range accessible to MD (Table S1). Specifically, changing the cooling rate by nearly two orders of magnitude alters absolute CTE values by less than 5%, while the ordering $\beta_{\mathrm{ico}} < \beta_{\mathrm{mixed}} < \beta_{\mathrm{crystal}}$ is preserved in both the glassy and liquid regimes. This consistency suggests that the structural trends reported here are robust within the framework of MD simulations, even if absolute values may differ from those measured experimentally.

Finally, the analysis based on the radial probability distribution function $G(r)$ overcomes the limitations of previous approaches that rely solely on the peak position of $g(r)$. Earlier studies reported apparent contraction upon heating [38, 42, 86, 87], often interpreted as negative thermal expansion (see also Fig. S11). However, such conclusions arise from neglecting the asymmetry of the first peak of $g(r)$. By fitting this peak using a skewed normal distribution and tracking the mean bond length Fig. 8 and Fig. 9, we revealed a continuous increase in the average interatomic distance with temperature. The change in slope around T_g corresponds to the structural transition from the amorphous to the liquid state. This trend is reproduced across all studied systems (Figs. S10-S12) and demonstrates that, for all investigated systems, the average nearest-neighbor distance in the first coordination shell increases monotonically with temperature when peak asymmetry is properly accounted for.

V. CONCLUSION

We investigated the structural behavior of a range of metallic glasses widely studied in the literature, including monoatomic MGs, binary, ternary, and high-entropy alloys. The radial distribution function (RDF) revealed enhanced short-range order and a splitting of the second RDF peak, confirming the formation of a metallic glassy state. The glass transition temperatures of the different systems were determined from the temperature dependence of the volume during cooling. The thermal responses of local atomic structures in MGs, both below and above the glass transition temperature, were analyzed. Voronoi tessellation analysis showed that mixed-like polyhedra are the primary contributors to macroscopic thermal expansion, whereas icosahedral-like polyhedra exhibit reduced local expansion and thus play a stabilizing role. Crystal-like motifs were found to play only a minor role due to their scarcity. These observations were corroborated by the potential energy analysis, which highlighted the energetic stability of icosahedral patterns and the anharmonic nature of mixed polyhedra. Contrary to previous studies suggesting an apparent contraction of interatomic bonds based on the position of the first maximum of $g(r)$, our analysis using the radial probability function $G(r)$, combined with the fitting by an asymmetric normal distribution suggested in Ref. [86], revealed a clear positive local expansion with increasing temperature. Taken together, the results across 25 metallic glass compositions spanning five chemical families, and validated against multiple interatomic potentials and cooling rates, reveal a robust, motif-dependent structural behavior governing thermal expansion. The consistent ordering $\beta_{\text{ico}} < \beta_{\text{mixed}} < \beta_{\text{crystal}}$ across all investigated systems suggests this is a general characteristic of MGs rather than a composition- or potential-specific artifact. These findings provide a consistent atomic-scale understanding of macroscopic thermal expansion and offer useful insights for the rational design of MGs with enhanced thermal stability.

DATA AVAILABILITY

The data is available from the corresponding author upon request.

CONFLICT OF INTEREST

The author declares that there are no known conflicts of interest.

[1] W. Klement, R. H. Willens, and P. Duwez, Non-crystalline structure in solidified gold–silicon alloys, Nature **187**, 869–870 (1960).

[2] Z. Xie, D. Chauraud, A. Atila, E. Bitzek, S. Korte-Kerzel, and J. Guénolé, Unveiling the mechanisms of motion of synchro-shockley dislocations in laves phases, Physical Review Materials **7**, 10.1103/physrevmaterials.7.053605 (2023).

[3] D. Şopu, X. Yuan, F. Spieckermann, and J. Eckert, Coupling structural, chemical composition and stress fluctuations with relaxation dynamics in metallic glasses, Acta Materialia **275**, 120033 (2024).

[4] Z. Xie, A. Atila, J. Guénolé, S. Korte-Kerzel, T. Al-Samman, and U. Kerzel, Predicting grain boundary segregation in magnesium alloys: An atomistically informed machine learning approach, Journal of Magnesium and Alloys **13**, 2636–2650 (2025).

[5] L. Tian, Y.-Q. Cheng, Z.-W. Shan, J. Li, C.-C. Wang, X.-D. Han, J. Sun, and E. Ma, Approaching the ideal elastic limit of metallic glasses, Nature Communications **3**, 10.1038/ncomms1619 (2012).

[6] A. Atila, S. V. Sukhomlinov, M. J. Honecker, and M. H. Müser, Plasticity of metallic glasses dictated by their state at the fragile-to-strong transition temperature, Acta Materialia **286**, 120753 (2025).

[7] L. Jiang, M. Bao, Y. Dong, Y. Yuan, X. Zhou, and X. Meng, Processing, production and anticorrosion behavior of metallic glasses: A critical review, Journal of Non-Crystalline Solids **612**, 122355 (2023).

[8] H. Li, Z. Lu, S. Wang, Y. Wu, and Z. Lu, Fe-based bulk metallic glasses: Glass formation, fabrication, properties and applications, Progress in Materials Science **103**, 235–318 (2019).

[9] X. Li, J. Zhou, L. Shen, B. Sun, H. Bai, and W. Wang, Exceptionally high saturation magnetic flux density and ultralow coercivity via an amorphous–nanocrystalline transitional microstructure in an feco-based alloy, Advanced Materials **35**, 10.1002/adma.202205863 (2022).

[10] MA, M and Liu, R and Xiao, Y and Lou, D and Liu, L and Wang, Q and Wang, W, Wear resistance of zr-based

bulk metallic glass applied in bearing rollers, Materials Science and Engineering A **386**, 326–330 (2004).
[11] Q. Jia, W. He, D. Hua, Q. Zhou, Y. Du, Y. Ren, Z. Lu, H. Wang, F. Zhou, and J. Wang, Effects of structure relaxation and surface oxidation on nanoscopic wear behaviors of metallic glass, Acta Materialia **232**, 117934 (2022).
[12] Z. Wang, M. Li, J. Yu, X. Ge, Y. Liu, and W. Wang, Low-iridium-content irnita metallic glass films as intrinsically active catalysts for hydrogen evolution reaction, Advanced Materials **32**, 10.1002/adma.201906384 (2019).
[13] R. Jiang, Y. Da, Z. Chen, X. Cui, X. Han, H. Ke, Y. Liu, Y. Chen, Y. Deng, and W. Hu, Progress and perspective of metallic glasses for energy conversion and storage, Advanced Energy Materials **12**, 10.1002/aenm.202101092 (2022).
[14] Y. Yan, C. Wang, Z. Huang, J. Fu, Z. Lin, X. Zhang, J. Ma, and J. Shen, Highly efficient and robust catalysts for the hydrogen evolution reaction by surface nano engineering of metallic glass, Journal of Materials Chemistry A **9**, 5415–5424 (2021).
[15] J. P. Singer, C. I. Pelligra, N. Kornblum, Y. Choo, M. Gopinadhan, P. Bordeenithikasem, J. Ketkaew, S. Fatt Liew, H. Cao, J. Schroers, and C. O. Osuji, Multiscale patterning of a metallic glass using sacrificial imprint lithography, Microsystems & Nanoengineering **1**, 10.1038/micronano.2015.40 (2015).
[16] A. Liens, A. Etiemble, P. Rivory, S. Balvay, J.-M. Pelletier, S. Cardinal, D. Fabrègue, H. Kato, P. Steyer, T. Munhoz, J. Adrien, N. Courtois, D. Hartmann, and J. Chevalier, On the potential of bulk metallic glasses for dental implantology: Case study on ti40zr10cu36pd14, Materials **11**, 249 (2018).
[17] B. Nair and B. Geetha Priyadarshini, Process, structure, property and applications of metallic glasses, AIMS Materials Science **3**, 1022–1053 (2016).
[18] L. Liu, C. Qiu, C. Huang, Y. Yu, H. Huang, and S. Zhang, Biocompatibility of ni-free zr-based bulk metallic glasses, Intermetallics **17**, 235–240 (2009).
[19] M. M. Khan, A. Nemati, Z. U. Rahman, U. H. Shah, H. Asgar, and W. Haider, Recent advancements in bulk metallic glasses and their applications: A review, Critical Reviews in Solid State and Materials Sciences **43**, 233–268 (2017).
[20] M. Zhu, J. Liu, Q. Huang, J. Dong, and X. Yang, Temperature and size modulation of the lattice thermal expansion on transition metallic nanostructures, Journal of Physics D: Applied Physics **55**, 485303 (2022).
[21] S. A. Kareem, J. U. Anaele, E. O. Aikulola, O. F. Olanrewaju, B. O. Omiyale, M. O. Bodunrin, and K. K. Alaneme, Hot deformation behaviour, constitutive model description, and processing map analysis of superalloys: An overview of nascent developments, Journal of Materials Research and Technology **26**, 8624–8669 (2023).
[22] S. Koric and B. G. Thomas, Efficient thermo-mechanical model for solidification processes, International Journal for Numerical Methods in Engineering **66**, 1955–1989 (2006).
[23] P. Sengupta and I. Manna, Advanced high-temperature structural materials for aerospace and power sectors: A critical review, Transactions of the Indian Institute of Metals **72**, 2043–2059 (2019).
[24] A. Klingler, M. Gilberg, D. Reisinger, S. Schlögl, B. Wetzel, and J.-K. Krüger, Thermal volume expansion as seen by temperature-modulated optical refractometry, oscillating dilatometry and thermo-mechanical analysis, Polymer Testing **131**, 108340 (2024).
[25] T. Lu, S. L. Liu, Y. H. Sun, W.-H. Wang, and M.-X. Pan, A free-volume model for thermal expansion of metallic glass, Chinese Physics Letters **39**, 036401 (2022).
[26] A. K. Gangopadhyay, C. E. Pueblo, and K. F. Kelton, Link between volume, thermal expansion, and bulk metallic glass formability, Physical Review Materials **4**, 10.1103/physrevmaterials.4.095602 (2020).
[27] H. Kato, H.-S. Chen, and A. Inoue, Relationship between thermal expansion coefficient and glass transition temperature in metallic glasses, Scripta Materialia **58**, 1106–1109 (2008).
[28] R. A. Wesolowski, A. P. Wesolowski, and R. S. Petrova, Crystalline and amorphous solids, in *The World of Materials* (Springer International Publishing, 2020) p. 31–38.
[29] Y. Hong, H. Wang, X. Li, L. Zhong, H. Chen, Z. Zhang, P. Cao, R. O. Ritchie, and J. Wang, Structural heterogeneity governing deformability of metallic glass, Matter **6**, 1160–1172 (2023).
[30] B. Shang, P. Guan, and J.-L. Barrat, Role of thermal expansion heterogeneity in the cryogenic rejuvenation of metallic glasses, Journal of Physics: Materials **1**, 015001 (2018).
[31] M. Okaji, N. Yamada, and H. Moriyama, Ultraprecise thermal expansion measurements of ceramic and steel gauge blocks with an interferometric dilatometer, Metrologia **37**, 165–171 (2000).
[32] F. Lanza di Scalea, Measurement of thermal expansion coefficients of composites using strain gages, Experimental Mechanics **38**, 233–241 (1998).
[33] Y. Liu, F. Sommer, and E. Mittemeijer, Calibration of the differential dilatometric measurement signal upon heating and cooling; thermal expansion of pure iron, Thermochimica Acta **413**, 215–225 (2004).
[34] X. Feng, C. Sun, X. Zhang, and F. Ansari, Determination of the coefficient of thermal expansion with embedded long-gauge fiber optic sensors, Measurement Science and Technology **21**, 065302 (2010).
[35] G. Singer, G. Sinn, H. C. Lichtenegger, S. Veigel, M. Zecchini, and R. Wan-Wendner, Evaluation of in-situ shrinkage and expansion properties of polymer composite materials for adhesive anchor systems by a novel approach based on digital image correlation, Polymer Testing **79**, 106035 (2019).
[36] A. H. Taghvaei, H. Shakur Shahabi, J. Bednarčik, and J. Eckert, Inhomogeneous thermal expansion of metallic glasses in atomic-scale studied by in-situ synchrotron x-ray diffraction, Journal of Applied Physics **117**, 10.1063/1.4906552 (2015).
[37] Y. Zhang, N. Mattern, and J. Eckert, Strong correlation of atomic thermal motion in the first coordination shell of a cu-zr metallic glass, Applied Physics Letters **102**, 10.1063/1.4792752 (2013).
[38] Y. Su, X. Wang, Q. Cao, D. Zhang, and J.-Z. Jiang, Different thermal responses of local structures in pd43cu27ni10p20 alloy from glass to liquid, The Journal of Physical Chemistry C **124**, 19817–19828 (2020).
[39] J. Ding and E. Ma, Computational modeling sheds light on structural evolution in metallic glasses and supercooled liquids, npj Computational Materials **3**, 10.1038/s41524-017-0007-1 (2017).

[40] N. Mattern, J. Bednarcik, M. Stoica, and J. Eckert, Temperature dependence of the short-range order of cu65zr35 metallic glass, Intermetallics **32**, 51–56 (2013).

[41] A. K. Gangopadhyay, M. E. Blodgett, M. L. Johnson, J. McKnight, V. Wessels, A. J. Vogt, N. A. Mauro, J. C. Bendert, R. Soklaski, L. Yang, and K. F. Kelton, Anomalous thermal contraction of the first coordination shell in metallic alloy liquids, The Journal of Chemical Physics **140**, 10.1063/1.4861666 (2014).

[42] S. Evertz, D. Music, V. Schnabel, J. Bednarcik, and J. M. Schneider, Thermal expansion of pd-based metallic glasses by ab initio methods and high energy x-ray diffraction, Scientific Reports **7**, 10.1038/s41598-017-16117-7 (2017).

[43] H. Li and Y. Zheng, Recent advances in bulk metallic glasses for biomedical applications, Acta Biomaterialia **36**, 1–20 (2016).

[44] Y. Zeng, A. Inoue, N. Nishiyama, and M. Chen, Ni-rich ni–pd–p bulk metallic glasses with significantly improved glass-forming ability and mechanical properties by si addition, Intermetallics **18**, 1790–1793 (2010).

[45] C. Zhu, Q. Wang, Y. Zhao, Y. Wang, J. Qiang, and C. Dong, Ni-based ni-fe-b-si-ta bulk metallic glasses, Science China Physics, Mechanics and Astronomy **53**, 440–444 (2010).

[46] A. P. Thompson, H. M. Aktulga, R. Berger, D. S. Bolintineanu, W. M. Brown, P. S. Crozier, P. J. in 't Veld, A. Kohlmeyer, S. G. Moore, T. D. Nguyen, R. Shan, M. J. Stevens, J. Tranchida, C. Trott, and S. J. Plimpton, Lammps - a flexible simulation tool for particle-based materials modeling at the atomic, meso, and continuum scales, Computer Physics Communications **271**, 108171 (2022).

[47] G. P. Purja Pun, V. Yamakov, and Y. Mishin, Interatomic potential for the ternary ni–al–co system and application to atomistic modeling of the b2–l10martensitic transformation, Modelling and Simulation in Materials Science and Engineering **23**, 065006 (2015).

[48] Y. Li, M. Lv, and H. Liang, Local structural arrangement of amorphous al-ni-co alloy during uniaxial tension: A molecular dynamics study, Materials Transactions **57**, 1505–1508 (2016).

[49] M. Kbirou, A. Hasnaoui, K. Saadouni, M. Badawi, and M. Mazroui, Pressure effects on local atomic structure of ni15co15al70 metallic glasses, Computational Materials Science **166**, 20–29 (2019).

[50] A. Atila, M. Kbirou, S. Ouaskit, and A. Hasnaoui, On the presence of nanoscale heterogeneity in al70ni15co15 metallic glass under pressure, Journal of Non-Crystalline Solids **550**, 120381 (2020).

[51] M. Kbirou, A. Atila, and A. Hasnaoui, On the structure and icosahedral interconnectivity in tantalum monatomic glass produced under pressure, Physica Scripta **99**, 085946 (2024).

[52] M. S. Daw, S. M. Foiles, and M. I. Baskes, The embedded-atom method: a review of theory and applications, Materials Science Reports **9**, 251–310 (1993).

[53] W.-M. Choi, Y. H. Jo, S. S. Sohn, S. Lee, and B.-J. Lee, Understanding the physical metallurgy of the cocrfemnni high-entropy alloy: an atomistic simulation study, npj Computational Materials **4**, 10.1038/s41524-017-0060-9 (2018).

[54] D. Tramontina, O. Deluigi, R. Pinzón, J. Rojas-Nunez, F. Valencia, R. Pasianot, S. Baltazar, R. Gonzalez, and E. Bringa, Probing radiation resistance in simulated metallic core–shell nanoparticles, Computational Materials Science **227**, 112304 (2023).

[55] M. I. Mendelev, F. Zhang, Z. Ye, Y. Sun, M. C. Nguyen, S. R. Wilson, C. Z. Wang, and K. M. Ho, Development of interatomic potentials appropriate for simulation of devitrification of al$_9$0sm$_1$0alloy, Modelling and Simulation in Materials Science and Engineering **23**, 045013 (2015).

[56] Y. Q. Cheng, E. Ma, and H. W. Sheng, Atomic level structure in multicomponent bulk metallic glass, Physical Review Letters **102**, 10.1103/physrevlett.102.245501 (2009).

[57] N. Leimeroth, J. Rohrer, and K. Albe, General purpose potential for glassy and crystalline phases of cu-zr alloys based on the ace formalism, Physical Review Materials **8**, 10.1103/physrevmaterials.8.043602 (2024).

[58] S. Nosé, A unified formulation of the constant temperature molecular dynamics methods, The Journal of Chemical Physics **81**, 511–519 (1984).

[59] `URL_will_be_inserted_by_publisher`.

[60] M. Wang, K. Zhang, Z. Li, Y. Liu, J. Schroers, M. D. Shattuck, and C. S. O'Hern, Asymmetric crystallization during cooling and heating in model glass-forming systems, Physical Review E **91**, 10.1103/physreve.91.032309 (2015).

[61] H. Kourbani, S. Bogtob, A. Samiri, A. Hassani, and A. Hasnaoui, Thermal nanoindentation of (3c) silicon carbide 3c-sic using molecular dynamics simulation, Solid State Communications **403**, 116013 (2025).

[62] A. Atila, E. M. Ghardi, S. Ouaskit, and A. Hasnaoui, Atomistic insights into the impact of charge balancing cations on the structure and properties of aluminosilicate glasses, Physical Review B **100**, 10.1103/physrevb.100.144109 (2019).

[63] J. Ding, Y.-Q. Cheng, and E. Ma, Full icosahedra dominate local order in cu64zr34 metallic glass and supercooled liquid, Acta Materialia **69**, 343–354 (2014).

[64] M. Kumar, E. Nicholson, D. W. Kirk, S. J. Thorpe, and C. V. Singh, Short-range structural origins of serration events in metallic glasses, Journal of Alloys and Compounds **787**, 840–850 (2019).

[65] M. Celtek, S. Sengul, and U. Domekeli, Glass formation and structural properties of zr50cu50-xalx bulk metallic glasses investigated by molecular dynamics simulations, Intermetallics **84**, 62–73 (2017).

[66] M. Tahiri, A. Hassani, K. Sbiaai, and A. Hasnaoui, Investigating local atomic structural order in $TiAl_3$ metallic glass using molecular dynamic simulation, Computational Condensed Matter **14**, 74–83 (2018).

[67] D. Turnbull and M. H. Cohen, On the free-volume model of the liquid-glass transition, The Journal of Chemical Physics **52**, 3038–3041 (1970).

[68] A. Khmich, K. Sbiaai, and A. Hasnaoui, Structural behavior of tantalum monatomic metallic glass, Journal of Non-Crystalline Solids **510**, 81–92 (2019).

[69] M. Tahiri, S. Trady, A. Hasnaoui, M. Mazroui, K. Saadouni, and K. Sbiaai, Structural properties of al and tial3 metallic glasses — an embedded atom method study, Modern Physics Letters B **30**, 1650170 (2016).

[70] A. R. Yavari, M. Tonegaru, N. Lupu, A. Inoue, E. Matsubara, G. Vaughan, Å. Kvick, and W. Botta, Quenched-in Free Volume V_f, Deformation-induced Free Volume, the Glass Transition Tg and Thermal Expansion in glassy ZrNbCuNiAl measured by Time-resolved Diffraction in

Transmission, MRS Proceedings **806**, 10.1557/proc-806-mm3.5 (2003).
[71] N. Mattern, H. Hermann, S. Roth, J. Sakowski, M.-P. Macht, P. Jovari, and J. Jiang, Structural behavior of pd40cu30ni10p20 bulk metallic glass below and above the glass transition, Applied Physics Letters **82**, 2589–2591 (2003).
[72] Q. Jiang, Z. Chang, X. Wang, and J. Jiang, Structures at glassy, supercooled liquid, and liquid states in la-based bulk metallic glasses, Metallurgical and Materials Transactions A **41**, 1634–1639 (2009).
[73] A. R. Yavari, A. L. Moulec, A. Inoue, N. Nishiyama, N. Lupu, E. Matsubara, W. J. Botta, G. Vaughan, M. D. Michiel, and Å. Kvick, Excess free volume in metallic glasses measured by x-ray diffraction, Acta Materialia **53**, 1611–1619 (2005).
[74] P. Lunkenheimer, A. Loidl, B. Riechers, A. Zaccone, and K. Samwer, Thermal expansion and the glass transition, Nature Physics **19**, 694–699 (2023).
[75] M. Potuzak, J. C. Mauro, T. J. Kiczenski, A. J. Ellison, and D. C. Allan, Communication: Resolving the vibrational and configurational contributions to thermal expansion in isobaric glass-forming systems, The Journal of Chemical Physics **133**, 10.1063/1.3481441 (2010).
[76] I.-R. Lu, G. Görler, H.-J. Fecht, and R. Willnecker, Investigation of specific heat and thermal expansion in the glass-transition regime of pd-based metallic glasses, Journal of Non-Crystalline Solids **274**, 294–300 (2000).
[77] T. Komatsu, K. Matusita, and R. Yokota, Compositional dependence of thermal expansion coefficient of metallic glasses, Journal of Non-Crystalline Solids **72**, 279–286 (1985).
[78] A. Hitit and H. Şahin, The effect of iron content on glass forming ability and thermal stability of co–fe–ni–ta–nb–b–si bulk metallic glass, Metals **7**, 7 (2016).
[79] Y. Cheng, J. Ding, and E. Ma, Local topology vs. atomic-level stresses as a measure of disorder: Correlating structural indicators for metallic glasses, Materials Research Letters **1**, 3–12 (2012).
[80] T. Fukunaga, K. Itoh, T. Otomo, K. Mori, M. Sugiyama, H. Kato, M. Hasegawa, A. Hirata, Y. Hirotsu, and A. C. Hannon, Voronoi analysis of the structure of ni-zr-al ternary metallic glass, Materials Transactions **48**, 1698–1702 (2007).
[81] A. Samiri, A. Khmich, H. Haouas, A. Hassani, and A. Hasnaoui, Structural and mechanical behaviors of mg-al metallic glasses investigated by molecular dynamics simulations, Computational Materials Science **184**, 109895 (2020).
[82] A. Khmich, K. Sbiaai, and A. Hasnaoui, Annealing effect on elastic and structural behavior of tantalum monatomic metallic glass, Materials Chemistry and Physics **243**, 122636 (2020).
[83] A. Foroughi, R. Tavakoli, and H. Aashuri, Molecular dynamics study of structural formation in cu50–zr50 bulk metallic glass, Journal of Non-Crystalline Solids **432**, 334–341 (2016).
[84] M. I. Aoki and K. Tsumuraya, Ab initio molecular dynamics studies on volume stability of voronoi polyhedra under pressures in a metal glass, The Journal of Chemical Physics **104**, 6719–6723 (1996).
[85] H. W. Sheng, W. K. Luo, F. M. Alamgir, J. M. Bai, and E. Ma, Atomic packing and short-to-medium-range order in metallic glasses, Nature **439**, 419–425 (2006).
[86] S. V. Sukhomlinov and M. H. Müser, Determination of accurate, mean bond lengths from radial distribution functions, The Journal of Chemical Physics **146**, 10.1063/1.4973804 (2017).
[87] A. K. Gangopadhyay and K. F. Kelton, A re-evaluation of thermal expansion measurements of metallic liquids and glasses from x-ray scattering experiments, The Journal of Chemical Physics **148**, 10.1063/1.5032319 (2018).
[88] H. Lou, X. Wang, Q. Cao, D. Zhang, J. Zhang, T. Hu, H.-k. Mao, and J.-Z. Jiang, Negative expansions of interatomic distances in metallic melts, Proceedings of the National Academy of Sciences **110**, 10068–10072 (2013).
[89] F. H. Stillinger and P. G. Debenedetti, Distinguishing vibrational and structural equilibration contributions to thermal expansion, The Journal of Physical Chemistry B **103**, 4052–4059 (1999).
[90] A. K. Gangopadhyay, C. E. Pueblo, R. Dai, M. L. Johnson, R. Ashcraft, D. Van Hoesen, M. Sellers, and K. F. Kelton, Correlation of the fragility of metallic liquids with the high temperature structure, volume, and cohesive energy, The Journal of Chemical Physics **146**, 10.1063/1.4981011 (2017).
[91] J. Guo, X. Bian, Y. Zhao, S. Zhang, T. Li, and C. Wang, Correlation between the fragility of supercooled liquids and thermal expansion in the glassy state for gd-based glass-forming alloys, Journal of Physics: Condensed Matter **19**, 116103 (2007).
[92] Y. C. Hu, F. X. Li, M. Z. Li, H. Y. Bai, and W. H. Wang, Five-fold symmetry as indicator of dynamic arrest in metallic glass-forming liquids, Nature Communications **6**, 10.1038/ncomms9310 (2015).
[93] M. Kbirou, S. Trady, A. Hasnaoui, and M. Mazroui, Cooling rate dependence and local structure in aluminum monatomic metallic glass, Philosophical Magazine **97**, 2753–2771 (2017).
[94] Y. J. Lü, Q. L. Bi, H. S. Huang, and H. H. Pang, Role of fivefold symmetry in the dynamical slowing down of metallic glass-forming liquids, Physical Review B **96**, 10.1103/physrevb.96.064301 (2017).
[95] A. Houba, M. El Ayoubi, A. Samiri, A. Atila, and A. Hasnaoui, Short and medium range order in the rapidly solidified metallic liquid ta: Atomic packing, connection modes, and pressure effect, Materialia **38**, 102270 (2024).
[96] Y. Sato, C. Nakai, M. Wakeda, and S. Ogata, Predictive modeling of time-temperature-transformation diagram of metallic glasses based on atomistically-informed classical nucleation theory, Scientific Reports **7**, 10.1038/s41598-017-06482-8 (2017).

Supplementary Materials to: Icosahedral Short-Range Order Suppresses Thermal Expansion in Metallic Glasses

Hajar Boutnala[1], Hayat Haouas[2], Achraf Atila[3,†], and Abdellatif Hasnaoui[1,‡]

[1]LS2ME Laboratory, Sultan Moulay Slimane University of Beni Mellal, Polydisciplinary faculty of Khouribga, B.P. 145, 25000 Khouribga, Morocco

[2]Laboratory of Inorganic Materials for Sustainable Energy Technologies (LIMSET), Mohammed VI Polytechnic University (UM6P), Benguerir 43150, Morocco

[3]Federal Institute of Materials Research and Testing (BAM), Unter den Eichen 87, Berlin 12205, Germany

*hajar.boutnala@usms.ac.ma †achraf.atila@bam.de ‡hasnaoui59@hotmail.com

I. EFFECT OF COOLING AND HEATING RATE ON THERMAL EXPANSION

To motivate the choice of the heating rate, additional simulations were performed on the binary $Ni_{75}Al_{25}$ metallic glass using four different heating rates: 10^{11} K/s, 5×10^{11} K/s, 10^{12} K/s and 5×10^{12} K/s. The results (Fig. S1) indicate that for 5×10^{11} K/s, 10^{12} K/s, and 5×10^{12} K/s, the thermal expansion behavior was nearly identical. However, at the lowest rate of 10^{11} K/s, a contraction appeared near the glass transition temperature (T_g), which is a clear signature of crystallization. Therefore, 5×10^{12} K/s was selected in this study, as it prevents crystallization and reduces computational cost. Previous studies have shown that extremely large heating rates are commonly used in molecular dynamics simulations of metallic glasses to avoid crystallization while remaining consistent with atomistic timescale limitations [60, 96].

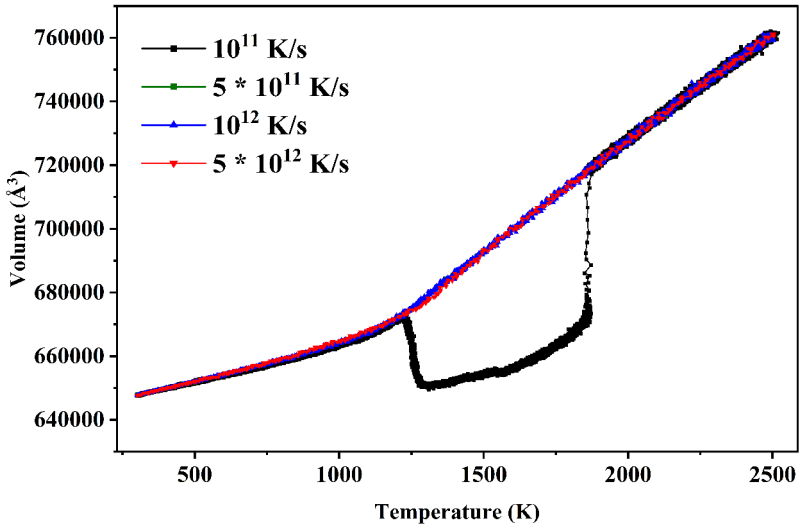

FIG. S1. Thermal expansion curves of the Ni_{75} Al_{25} metallic glass obtained with different heating rates (10^{11} K/s, 5×10^{11} K/s, 10^{12} K/s and 5×10^{12} K/s).

In Tab. S1 we show the sensitivity of the results to the cooling rate by redoing the same simulations for a selected composition (i.e., $Fe_{50}Ni_{30}Co_{10}Cr_{10}Mn_{10}$) using four different cooling rates that span almost 2 order of magnitude. As shown in Tab. S1, changing the cooling rate changed the values of CTE only marginally and, more importantly, the ordering where $\beta_{\text{ico}} < \beta_{\text{mixed}} < \beta_{\text{crystal}}$ is preserved across all cooling rates tested. While MD cooling rates remain orders of magnitude higher than experimental rates, the motif-dependent trends of local CTEs are robust within the range accessible to MD simulations.

II. EFFECT OF INTERATOMIC POTENTIAL ON LOCAL CTES

To address potential dependence, we performed additional simulations for two alloys using alternative interatomic potentials. For $Fe_{75}Ni_{25}$, we compared results from an EAM potential by Tramontina et al. [54] and a MEAM potential parametrized by Choi et al. [53]. For $Zr_{35}Cu_{65}$ system, we compared an EAM potential [56] with a machine learning

TABLE S1. Effect of cooling rate on global and local volumetric thermal expansion coefficients β_G (glass) and β_L (liquid), given in units of ($\times 10^{-5}$ K^{-1}).

	Glass β_G				Liquid β_L			
Cooling rate	Global	Crystal-like	Mixed-like	Icosahedral-like	Global	Crystal-like	Mixed-like	Icosahedral-like
5×10^{11}	4.17 ± 0.053	4.86 ± 0.022	4.35 ± 0.01	3.98 ± 0.04	8.01 ± 0.07	10.5 ± 0.02	7.58 ± 0.06	6.58 ± 0.01
10^{12}	4.19 ± 0.07	5.05 ± 0.02	4.41 ± 0.01	3.95 ± 0.08	7.90 ± 0.08	9.91 ± 0.02	7.65 ± 0.09	6.91 ± 0.02
5×10^{12}	4.12 ± 0.03	4.68 ± 0.006	4.40 ± 0.07	3.87 ± 0.04	7.83 ± 0.01	9.84 ± 0.02	7.45 ± 0.01	6.67 ± 0.01
10^{13}	4.20 ± 0.04	4.82 ± 0.02	4.56 ± 0.08	3.87 ± 0.03	7.95 ± 0.07	10.10 ± 0.03	7.54 ± 0.07	6.70 ± 0.06

potential [57], which offers a near-DFT level accuracy. In all cases, the ordering $\beta_{\text{ico}} < \beta_{\text{mixed}} < \beta_{\text{crystal}}$ is preserved for both liquid and glassy domains. Numerical values for these simulations are summarized in Tab. S2 and Tab. S3. Although absolute values are slightly different between potential, which is expected, the trends are consistent, which demonstrates that the main finding of this work, that is the icosahedral-like polyhedra are consistently associated with lower thermal expansion, is robust with respect to the choice of interatomic potential.

TABLE S2. Comparison of volumetric thermal expansion coefficients (K^{-1}) for $Fe_{75}Ni_{25}$ obtained using EAM and MEAM interaction models.

Potential	Global	Crystal-like	Mixed-like	Icosahedral-like
Glass regime				
EAM	4.61	5.19	4.84	4.23
MEAM	4.36	4.80	4.62	4.09
Liquid regime				
EAM	9.09	10.30	8.37	7.20
MEAM	7.85	9.58	7.41	6.75

TABLE S3. Comparison of volumetric thermal expansion coefficients ($\times 10^{-5}$ K^{-1}) for $Cu_{65}Zr_{35}$ obtained using EAM and ML interaction models.

Potential	Global	Crystal-like	Mixed-like	Icosahedral-like
Glass regime				
EAM	4.78	17.05	7.24	4.80
ML	5.40	19.22	7.65	4.88
Liquid regime				
EAM	7.90	27.28	10.14	8.17
ML	8.01	25.72	9.83	9.34

III. EFFECT OF INTERMEDIATE NPT RELAXATIONS DURING HEATING

In addition to the rate effect, we examined the influence of intermediate NPT relaxations during heating. For this purpose, a stepwise heating protocol was applied, in which the temperature was increased in increments of 100 K. At each temperature step, the system was relaxed under NPT conditions for 100 ps, and the average volume obtained during this relaxation was recorded. The results were compared with those obtained using the direct continuous heating protocol at the same effective heating rate of 5×10^{12} K/s. As shown in Fig. S2, no significant difference is observed in the global volume evolution between the two protocols. This comparison demonstrates that intermediate NPT relaxations do not significantly affect the macroscopic thermal expansion behavior under the present simulation conditions. Therefore, the direct heating protocol without intermediate relaxations was adopted in the main text for simplicity and computational efficiency.

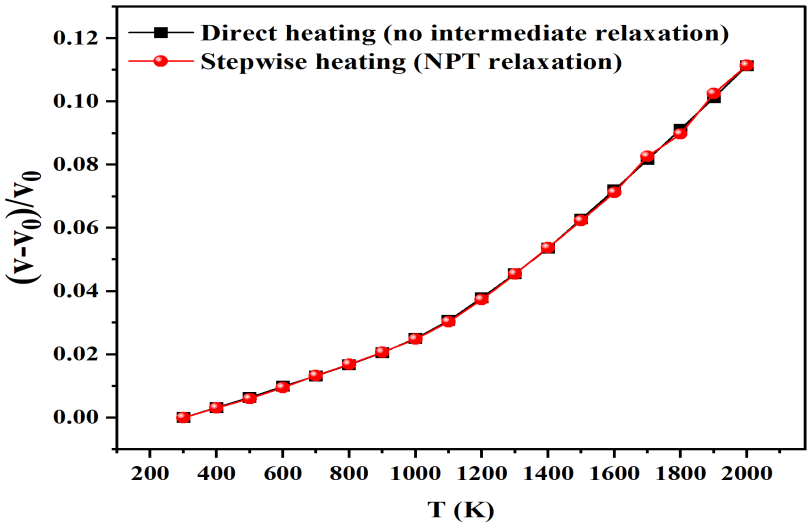

FIG. S2. Comparison of the global volume evolution obtained using (i) a stepwise heating protocol with intermediate NPT relaxations of 100 ps at each 100 K increment and (ii) a direct continuous heating protocol without intermediate relaxations for the $Ni_{70}Al_{20}Co_{10}$ metallic glass, both performed at an effective heating rate of 5×10^{12} K/s.

IV. STRUCTURAL FORMATION AND EVOLUTION OF METALLIC GLASSES

A. Radial distribution function

Fig. 1 presents the evolution of the radial distribution function during cooling.

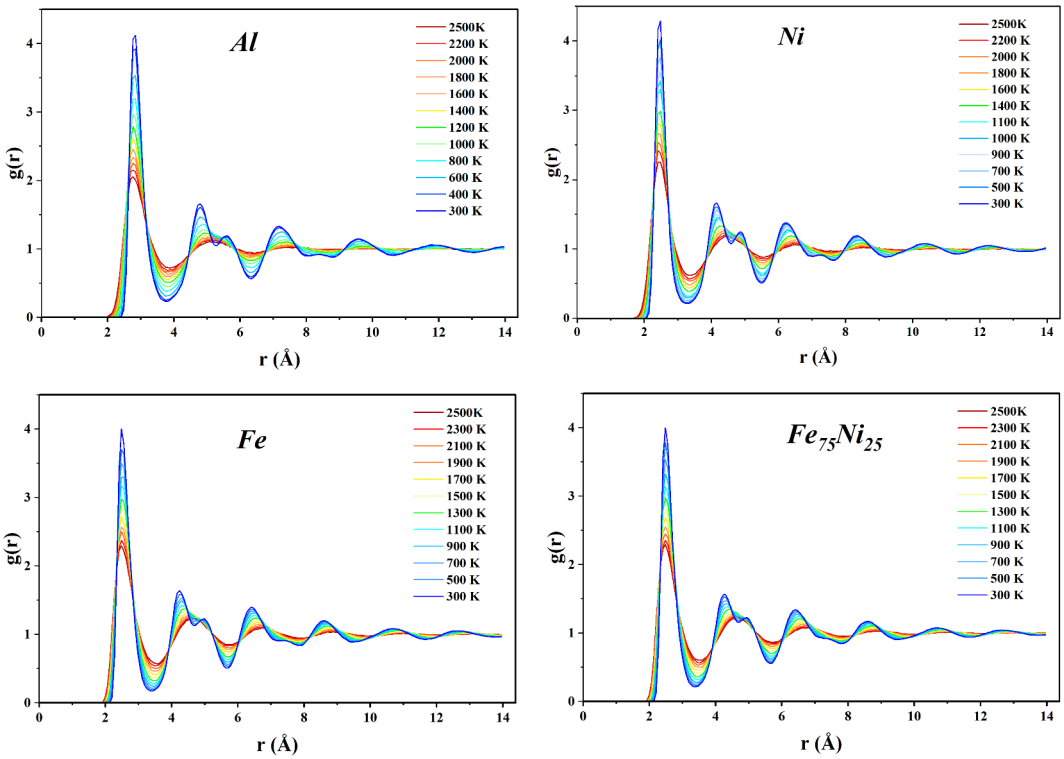

FIG. S3. Evolution of the total radial distribution function of the studied *MGs* during the cooling process.

B. Volume as a function of temperature

Fig. S4 shows the evolution of the total volume with temperature during heating and cooling.

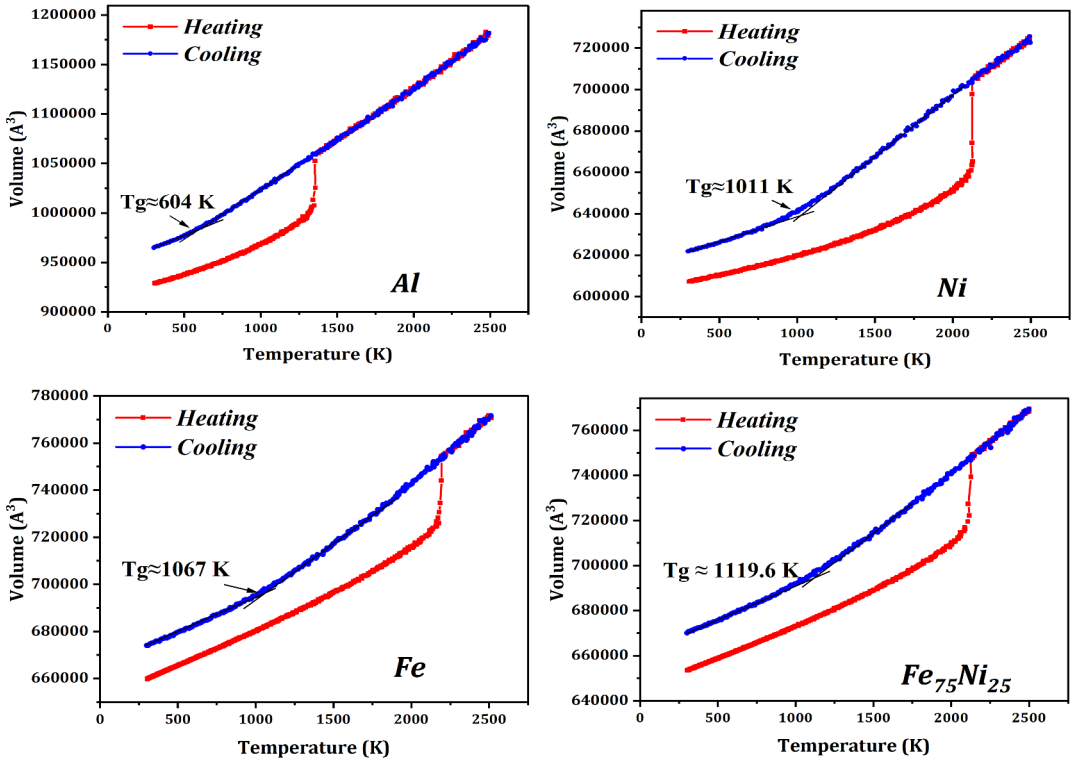

FIG. S4. Volume variation as a function of temperature for selected metallic systems during heating and cooling processes.

V. INVESTIGATION OF THERMAL EXPANSION IN METALLIC GLASSES

1. *Voronoi tessellation analysis*

Voronoi polyhedra are known to be unstable with regard to small perturbations of the particle positions, particularly under the effect of thermal vibrations, which can lead to topological instabilities and the formation of quasi-degenerate faces. In order to limit these effects, a filtering criterion based on minimum face area and minimum edge length is applied. The very small faces resulting from Voronoi tessellation are generally considered physically insignificant and are often attributed to numerical artifacts rather than actual structural features. In order to determine an appropriate surface threshold for filtering quasi-degenerate Voronoi faces, we calculated the histogram of face areas for all Voronoi polyhedra in the system using Ovito software. As shown in Fig. S5, the area distribution exhibits a marked minimum between the first narrow peak (corresponding to very small, probably non-physical faces) and the second broader peak (associated with significant atomic interfaces). This minimum was chosen as the filtering threshold, allowing digital artifacts to be eliminated while retaining relevant structural features.

2. *Classification of Voronoi polyhedra*

In order to analyze the structural contributions to thermal expansion, all Voronoi polyhedra were classified into three categories according to their topology:

Icosahedral-like: Voronoi polyhedra with a high degree of fivefold symmetry, defined as those having a number of pentagonal faces $n_5 \geq 8$. These structures are typically associated with local atomic packing that promotes glass formation.

Crystal-like: This class of polyhedra corresponds to those typically observed in crystalline phases. To define the relevant Voronoi indices, we first constructed reference crystal structures (e.g., FCC, BCC, HCP), then introduced moderate thermal perturbation by slightly increasing the temperature in these crystal systems. This procedure induced

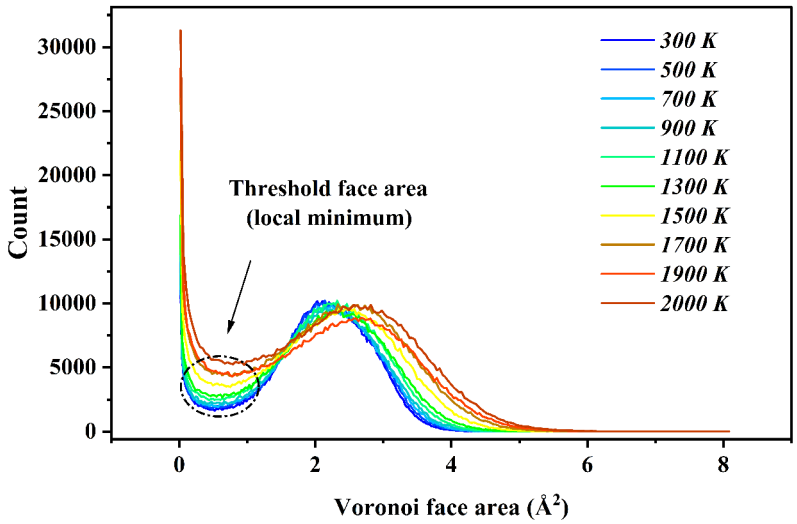

FIG. S5. Distribution of Voronoi face areas for $Ni_{75}Al_{25}$ at different temperatures. The minimum between the first narrow peak (artifacts) and the second broader peak (physical faces) is chosen as the threshold for filtering quasi-degenerate Voronoi faces.

small distortions in the polyhedra while preserving the overall crystal order. The Voronoi polyhedra generated under these conditions can thus be regarded as deformed crystalline motifs. The corresponding indices were then used as a reference to define the crystal-like category. The following indices were identified as representative of crystal-like Voronoi polyhedra in our analysis:

$$\langle 0,2,4,6\rangle,\ \langle 0,1,6,5\rangle,\ \langle 0,2,6,4\rangle,\ \langle 0,1,4,7\rangle,\ \langle 0,0,6,6\rangle,$$
$$\langle 0,9,4,0\rangle,\ \langle 0,9,2,1\rangle,\ \langle 0,8,4,0\rangle,\ \langle 0,0,4,8\rangle,\ \langle 0,3,4,6\rangle,$$
$$\langle 0,11,1,0\rangle,\ \langle 1,9,3,0\rangle,\ \langle 0,7,4,1\rangle,\ \langle 0,7,6,0\rangle,\ \langle 0,6,6,0\rangle,$$
$$\langle 0,4,4,6\rangle,\ \langle 0,6,0,8\rangle,\ \langle 0,12,0,0\rangle,\ \langle 0,10,2,0\rangle,\ \langle 0,9,3,0\rangle,$$
$$\langle 0,5,2,6\rangle,\ \langle 0,5,0,8\rangle,\ \langle 0,4,2,8\rangle.$$

Mixed-like: All remaining polyhedra that do not meet the criteria for icosahedral-like or crystal-like categories are grouped together in this class.

3. Fraction of Each Voronoi Polyhedron Type

To characterize the temperature-induced evolution of local atomic structures, we analyzed the fraction of each class of Voronoi polyhedra as a function of temperature.

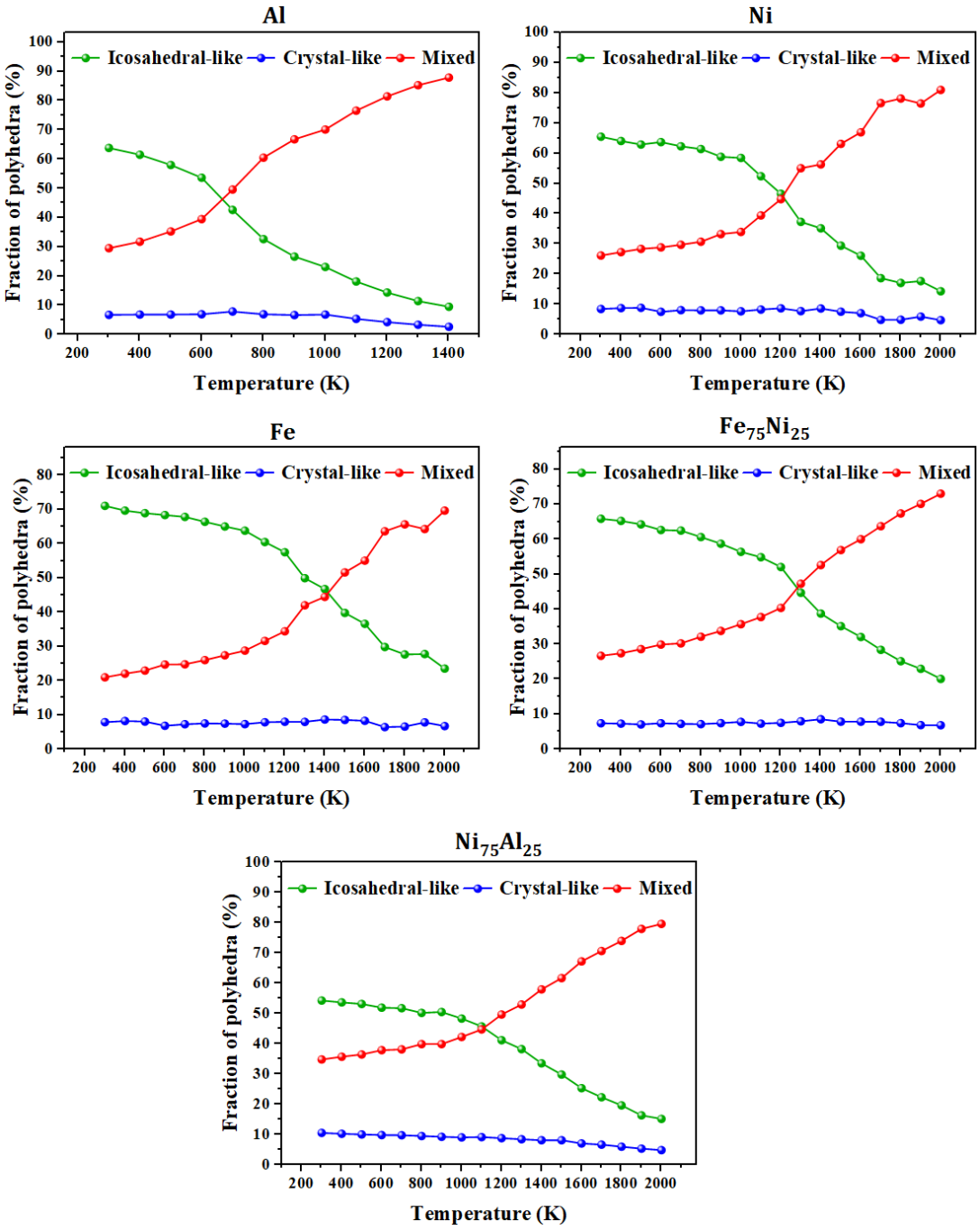

FIG. S6. Evolution of icosahedral-like, crystal-like, and mixed-like Voronoi polyhedra with temperature in selected metallic glasses.

4. Temperature Dependence of Average Atomic Volume for Different Voronoi Polyhedron Types

Fig. S7 summarizes the temperature dependence of the average atomic volume for different Voronoi polyhedron types.

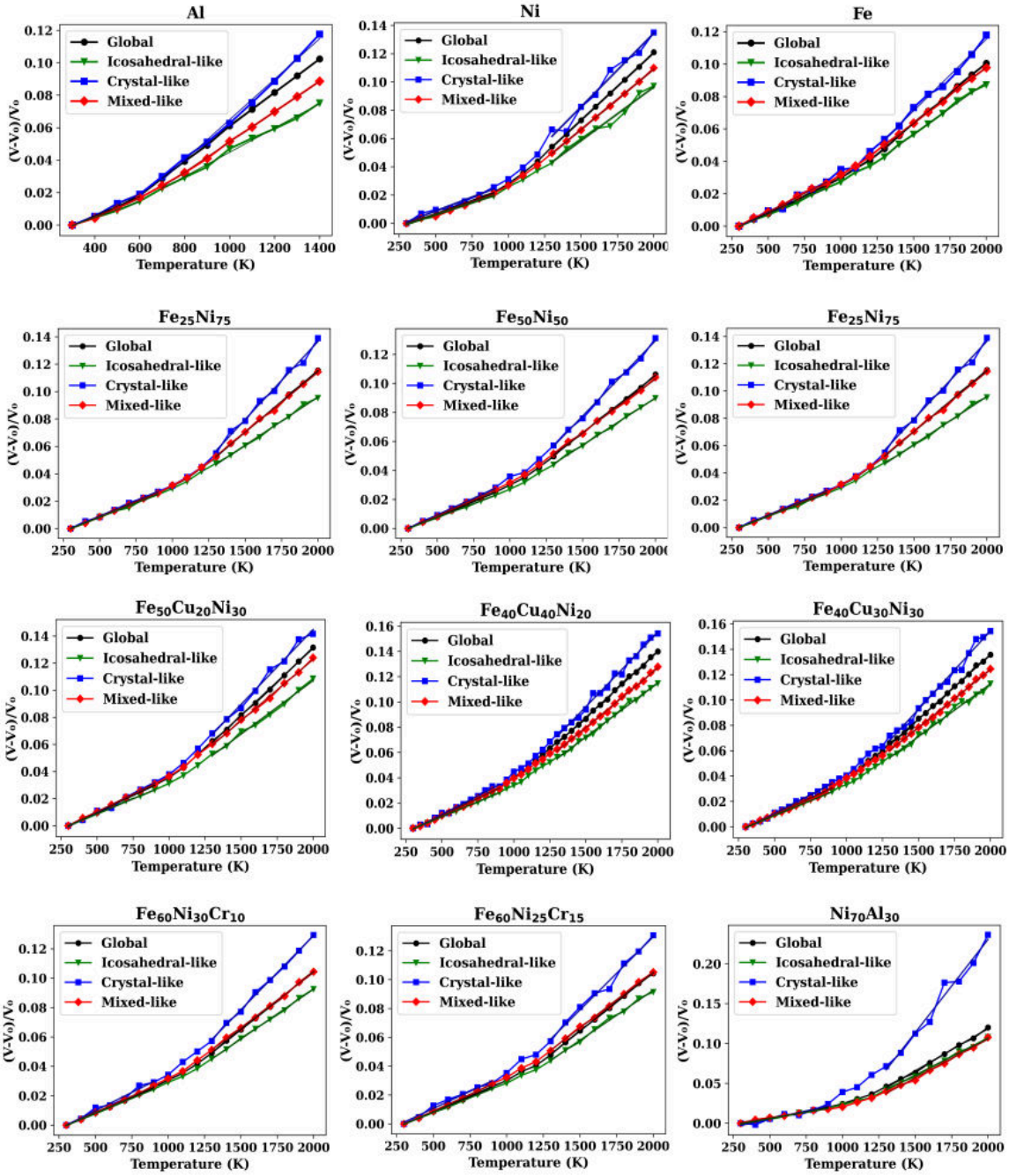

FIG. S7. Variation of global volume and atomic volume of icosahedral-like, crystal-like, and mixed-like Voronoi polyhedra during heating. The title on top of each plot indicates the sample for which the data is shown.

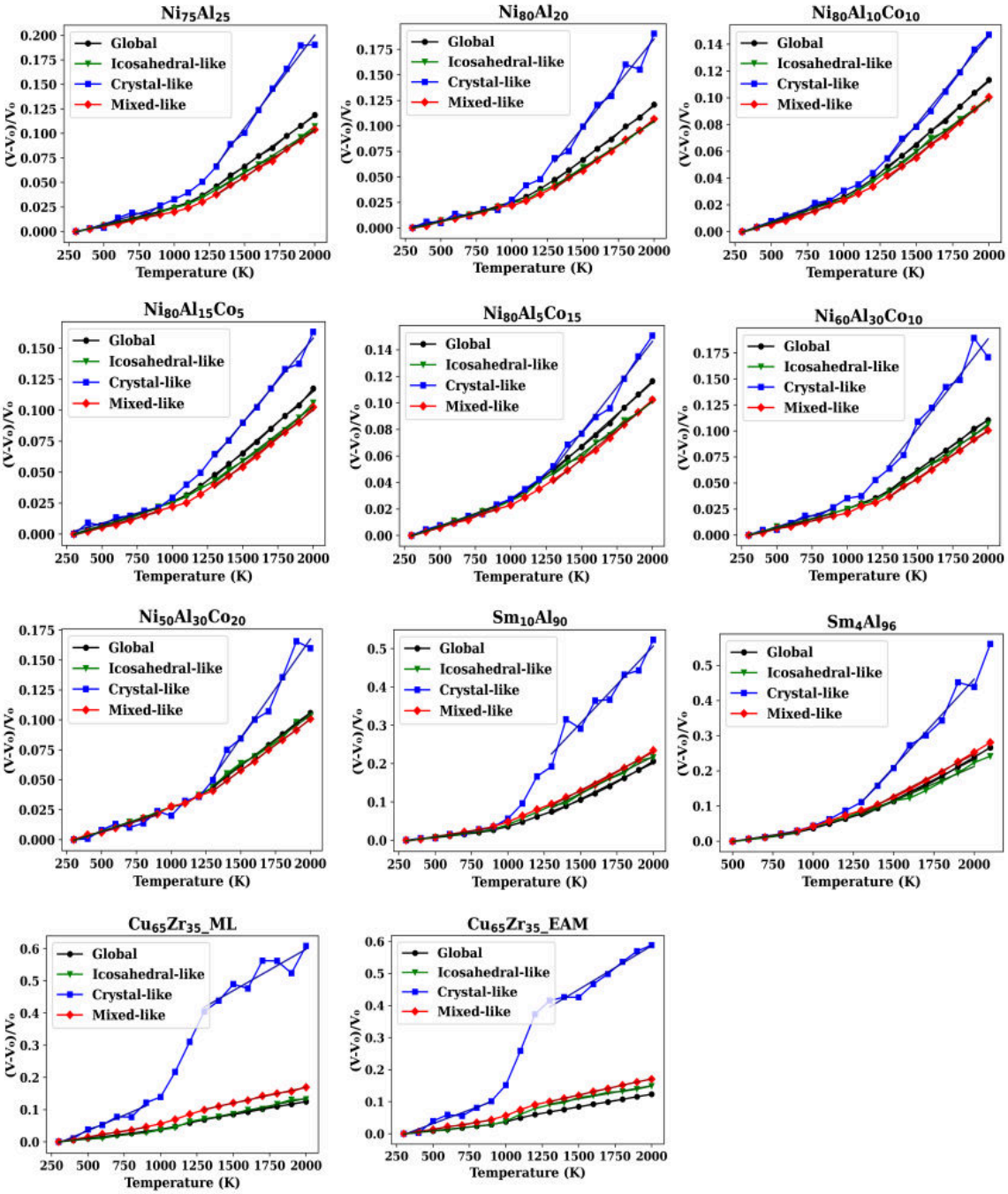

FIG. S8. Variation of global volume and atomic volume of icosahedral-like, crystal-like, and mixed-like Voronoi polyhedra during heating. The title on top of each plot indicates the sample for which the data is shown.

TABLE S4. Comparison between local and global coefficients of thermal expansion (β_G and β_L) in the glassy and liquid states for selected metallic systems.

System / Polyhedra	β_G ($10^{-5}\,\mathrm{K}^{-1}$)	β_L ($10^{-5}\,\mathrm{K}^{-1}$)	β_L/β_G
Al			
Global	6.07 ± 0.34	10.50 ± 0.13	1.72
Crystal-like	6.49 ± 0.35	13.30 ± 0.28	2.04
Mixed-like	5.64 ± 0.35	9.44 ± 0.10	1.67
Icosahedral-like	4.86 ± 0.24	7.40 ± 0.39	1.52
Ni			
Global	3.68 ± 0.24	9.54 ± 0.05	2.59
Crystal-like	3.91 ± 0.30	10.40 ± 0.68	2.65
Mixed-like	3.53 ± 0.20	8.54 ± 0.09	2.41
Icosahedral-like	3.38 ± 0.16	7.58 ± 0.44	2.24
Fe			
Global	4.20 ± 0.09	7.51 ± 0.06	1.78
Crystal-like	4.56 ± 0.26	8.84 ± 0.32	1.93
Mixed-like	4.44 ± 0.10	6.86 ± 0.06	1.54
Icosahedral-like	3.93 ± 0.11	6.46 ± 0.15	1.64
$Fe_{75}Ni_{25}$			
Global	4.36 ± 0.10	7.85 ± 0.06	1.80
Crystal-like	5.24 ± 0.15	9.41 ± 0.24	1.79
Mixed-like	4.73 ± 0.34	7.45 ± 0.08	1.57
Icosahedral-like	4.02 ± 0.10	6.98 ± 0.09	1.73

TABLE S5. (Table S4 Continued) Local and global CTE in glassy and liquid states.

System / Polyhedra	β_G ($10^{-5}\,\mathrm{K}^{-1}$)	β_L ($10^{-5}\,\mathrm{K}^{-1}$)	β_L/β_G
$Fe_{50}Ni_{50}$			
Global	4.16 ± 0.04	7.91 ± 0.12	1.90
Crystal-like	4.61 ± 0.06	10.39 ± 0.29	2.25
Mixed-like	4.44 ± 0.07	7.36 ± 0.14	1.66
Icosahedral-like	3.81 ± 0.06	6.49 ± 0.11	1.70
$Fe_{25}Ni_{75}$			
Global	4.35 ± 0.05	8.98 ± 0.13	2.06
Crystal-like	4.48 ± 0.11	11.37 ± 0.44	2.54
Mixed-like	4.38 ± 0.04	8.75 ± 0.16	2.00
Icosahedral-like	4.15 ± 0.15	7.04 ± 0.15	1.70
$Fe_{50}Cu_{20}Ni_{30}$			
Global	5.00 ± 0.06	9.92 ± 0.10	1.98
Crystal-like	5.39 ± 0.20	11.13 ± 0.43	2.07
Mixed-like	5.11 ± 0.04	9.04 ± 0.16	1.77
Icosahedral-like	4.45 ± 0.07	7.90 ± 0.25	1.78
$Fe_{40}Cu_{40}Ni_{20}$			
Global	5.42 ± 0.06	10.42 ± 0.10	1.92
Crystal-like	5.90 ± 0.18	11.79 ± 0.29	2.00
Mixed-like	5.39 ± 0.09	9.41 ± 0.12	1.75
Icosahedral-like	4.76 ± 0.04	8.59 ± 0.13	1.80

TABLE S6. (Table S4 Continued) Local and global CTE in glassy and liquid states.

System / Polyhedra	β_G ($10^{-5}\,\mathrm{K}^{-1}$)	β_L ($10^{-5}\,\mathrm{K}^{-1}$)	β_L/β_G
	$Fe_{40}Cu_{30}Ni_{30}$		
Global	5.22 ± 0.08	10.18 ± 0.10	1.95
Crystal-like	5.83 ± 0.24	12.36 ± 0.36	2.12
Mixed-like	5.10 ± 0.14	9.12 ± 0.11	1.79
Icosahedral-like	4.70 ± 0.05	8.32 ± 0.22	1.77
	$Fe_{60}Ni_{25}Cr_{15}$		
Global	4.32 ± 0.05	8.10 ± 0.07	1.88
Crystal-like	4.76 ± 0.30	10.10 ± 0.44	2.12
Mixed-like	4.63 ± 0.07	7.77 ± 0.10	1.68
Icosahedral-like	4.10 ± 0.06	6.95 ± 0.19	1.70
	$Fe_{60}Ni_{30}Cr_{10}$		
Global	4.31 ± 0.05	7.91 ± 0.08	1.83
Crystal-like	4.94 ± 0.33	10.01 ± 0.19	2.03
Mixed-like	4.47 ± 0.08	7.54 ± 0.12	1.69
Icosahedral-like	4.11 ± 0.04	6.79 ± 0.08	1.65
	$Ni_{70}Al_{30}$		
Global	3.34 ± 0.06	10.58 ± 0.23	3.17
Crystal-like	4.06 ± 0.53	23.37 ± 1.40	5.76
Mixed-like	2.91 ± 0.14	9.69 ± 0.31	3.33
Icosahedral-like	3.25 ± 0.18	9.32 ± 0.23	2.87

TABLE S7. (Table S4 Continued) Local and global CTE in glassy and liquid states.

System / Polyhedra	β_G ($10^{-5}\,\mathrm{K}^{-1}$)	β_L ($10^{-5}\,\mathrm{K}^{-1}$)	β_L/β_G
	$Ni_{75}Al_{25}$		
Global	3.44 ± 0.05	10.30 ± 0.15	2.99
Crystal-like	2.47 ± 0.64	17.80 ± 0.72	7.20
Mixed-like	3.37 ± 0.14	9.40 ± 0.10	2.78
Icosahedral-like	3.34 ± 0.10	9.08 ± 0.39	2.71
	$Ni_{80}Al_{20}$		
Global	3.51 ± 0.11	10.48 ± 0.16	2.99
Crystal-like	3.00 ± 0.48	17.21 ± 0.12	5.74
Mixed-like	3.35 ± 0.17	9.48 ± 0.21	2.83
Icosahedral-like	3.33 ± 0.16	9.02 ± 0.18	2.71
	$Ni_{80}Al_5Co_{15}$		
Global	3.75 ± 0.08	9.57 ± 0.20	2.55
Crystal-like	3.60 ± 0.25	13.72 ± 0.74	3.81
Mixed-like	3.33 ± 0.11	8.70 ± 0.21	2.61
Icosahedral-like	3.62 ± 0.08	7.84 ± 0.26	2.17
	$Ni_{80}Al_{10}Co_{10}$		
Global	3.70 ± 0.14	9.33 ± 0.18	2.52
Crystal-like	3.97 ± 0.26	13.28 ± 0.38	3.35
Mixed-like	3.22 ± 0.18	8.47 ± 0.24	2.63
Icosahedral-like	3.61 ± 0.09	7.85 ± 0.19	2.17

TABLE S8. (Table S4 Continued) Local and global CTE in glassy and liquid states.

System / Polyhedra	β_G ($10^{-5}\,K^{-1}$)	β_L ($10^{-5}\,K^{-1}$)	β_L/β_G
	$Ni_{80}Al_{15}Co_5$		
Global	3.55 ± 0.12	9.83 ± 0.22	2.77
Crystal-like	3.23 ± 0.42	13.64 ± 0.57	4.22
Mixed-like	3.13 ± 0.16	8.90 ± 0.26	2.84
Icosahedral-like	3.56 ± 0.12	8.74 ± 0.29	2.46
	$Ni_{60}Al_{30}Co_{10}$		
Global	3.49 ± 0.06	9.65 ± 0.10	2.77
Crystal-like	4.31 ± 0.40	17.26 ± 0.18	4.00
Mixed-like	3.09 ± 0.10	9.06 ± 0.19	2.93
Icosahedral-like	3.47 ± 0.11	9.11 ± 0.24	2.63
	$Ni_{50}Al_{30}Co_{20}$		
Global	3.70 ± 0.09	8.87 ± 0.10	2.40
Crystal-like	3.54 ± 0.50	16.48 ± 0.13	4.66
Mixed-like	3.55 ± 0.13	8.54 ± 0.06	2.41
Icosahedral-like	3.87 ± 0.11	8.37 ± 0.30	2.16
	Sm_4Al_{96}		
Global	6.15 ± 0.48	23.27 ± 0.20	3.78
Crystal-like	7.40 ± 0.41	50.00 ± 0.33	6.76
Mixed-like	7.13 ± 0.50	23.89 ± 0.07	3.35
Icosahedral-like	6.67 ± 0.76	19.57 ± 0.13	2.93
	$Sm_{10}Al_{90}$		
Global	4.43 ± 0.21	18.81 ± 0.57	4.25
Crystal-like	5.89 ± 0.51	40.17 ± 0.45	6.82
Mixed-like	6.11 ± 0.37	19.88 ± 0.56	3.25
Icosahedral-like	4.63 ± 0.29	19.26 ± 0.87	4.16
	$Cu_{65}Zr_{35}$ ML		
Global	5.40 ± 0.05	8.01 ± 0.10	1.48
Crystal-like	5.89 ± 0.51	25.71 ± 0.46	4.36
Mixed-like	6.11 ± 0.23	9.83 ± 0.27	1.61
Icosahedral-like	4.63 ± 0.29	9.34 ± 0.52	2.02
	$Cu_{65}Zr_{35}$ EAM		
Global	4.78 ± 0.07	7.90 ± 0.06	1.65
Crystal-like	17.05 ± 0.17	27.27 ± 2.20	1.60
Mixed-like	7.24 ± 0.22	10.14 ± 0.13	1.40
Icosahedral-like	4.80 ± 0.20	8.17 ± 0.50	1.70

5. *Potential Energy*

Figure S9 and Fig. S10 shows the evolution of the average atomic potential energy for the global system and for different Voronoi polyhedron types as a function of temperature.

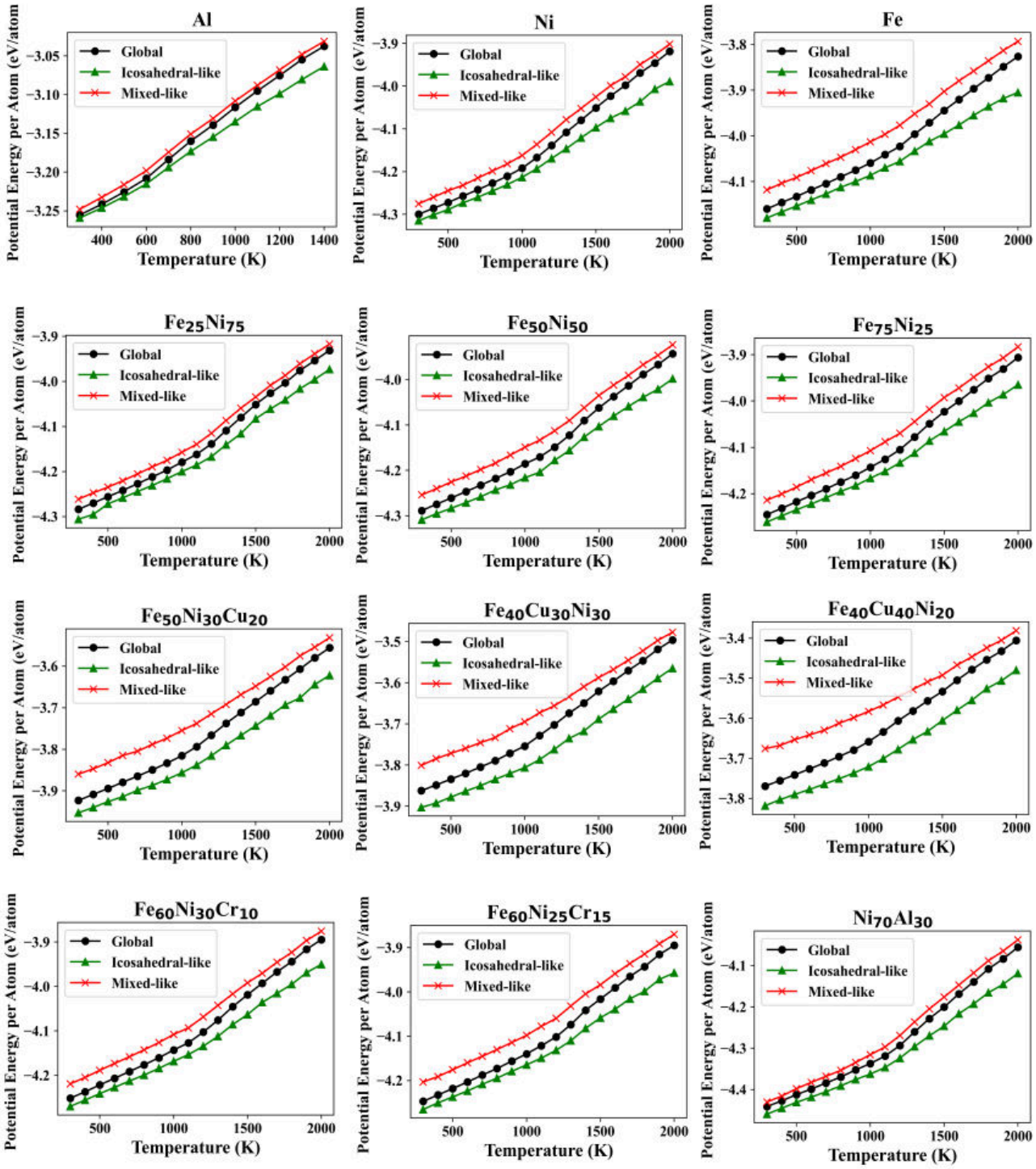

FIG. S9. Average atomic potential energy of the global system and of icosahedral-like, crystal-like, and mixed-like Voronoi polyhedra as a function of temperature. The title on top of each plot indicates the sample for which the data is shown.

6. *Local thermal expansion from the first peak position of $g(r)$*

For comparison with conventional analyses reported in the literature, the local thermal expansion was also estimated from the temperature dependence of the position of the first maximum of the radial distribution function $g(r)$. As shown in Fig. S11 for the $Fe_{50}Ni_{20}Co_{10}Cr_{10}Mn_{10}$ metallic glass, this approach yields an apparent decrease of the peak position in the liquid state, leading to an apparent negative local thermal expansion, in agreement with previous reports. As discussed in the main text, this behavior originates from the asymmetric shape of the first peak and the density-normalized nature of g(r), and therefore does not represent the true evolution of the average bond length. These limitations motivate the use of the radial probability distribution function $G(r) = 4\pi r^2 \rho\, g(r)$, combined with asymmetric peak fitting, as employed in the main text to obtain a physically meaningful local thermal expansion.

7. *Local thermal expansion, determined by the shift of the first peak of $G(r)$*

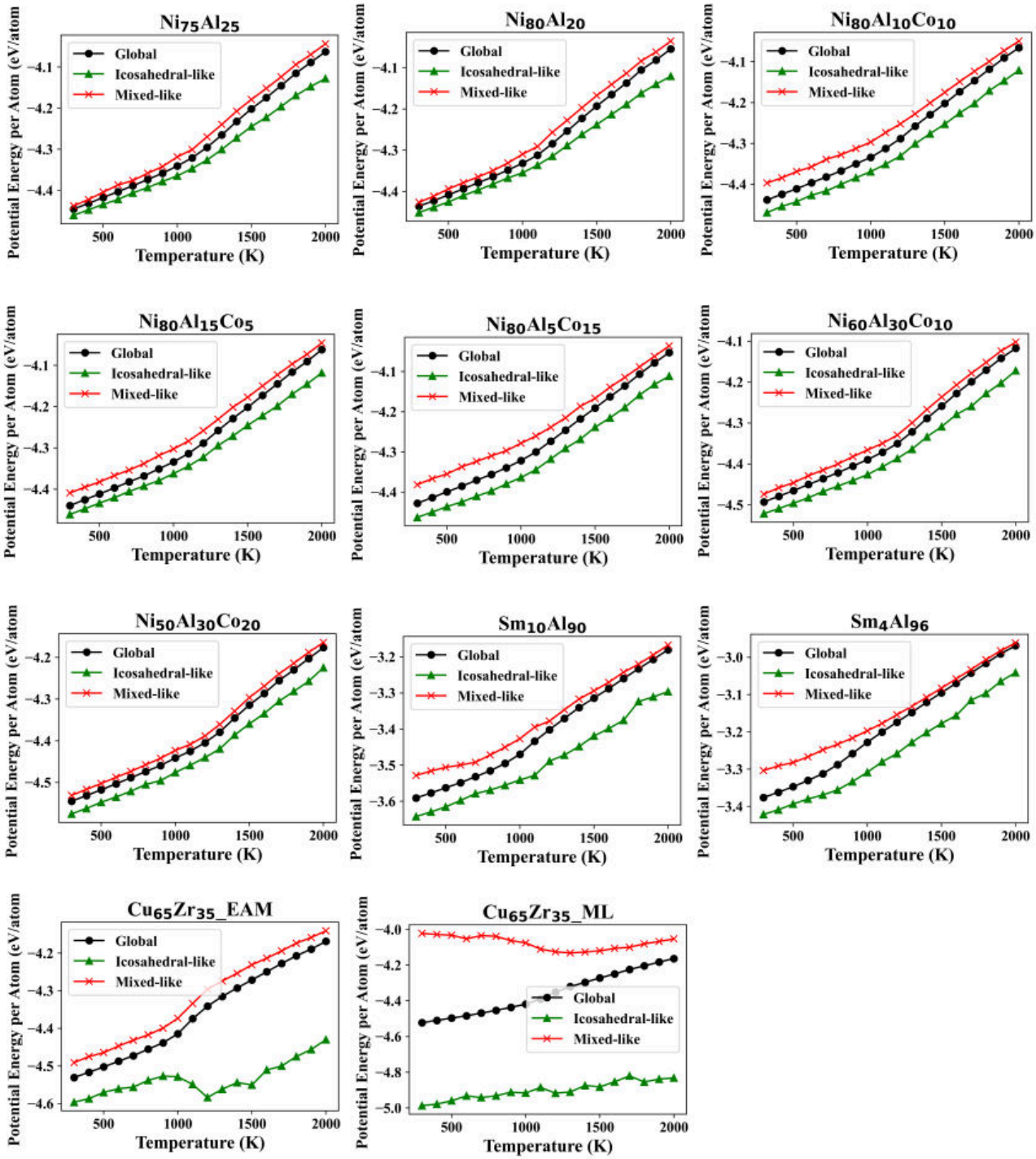

FIG. S10. Average atomic potential energy of the global system and of icosahedral-like, crystal-like, and mixed-like Voronoi polyhedra as a function of temperature. The title on top of each plot indicates the sample for which the data is shown.

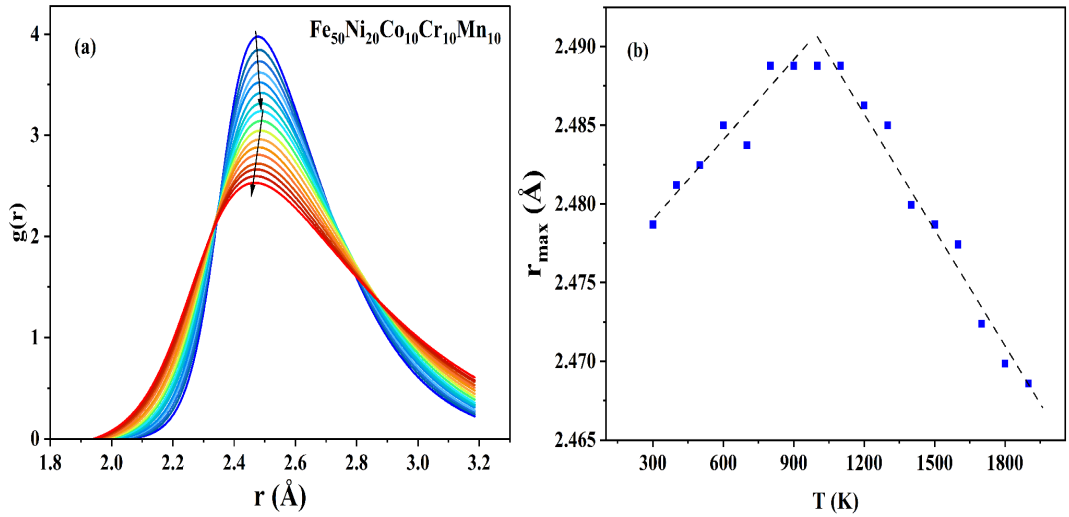

FIG. S11. Relative change of the mean nearest-neighbor distance with temperature for selected systems.

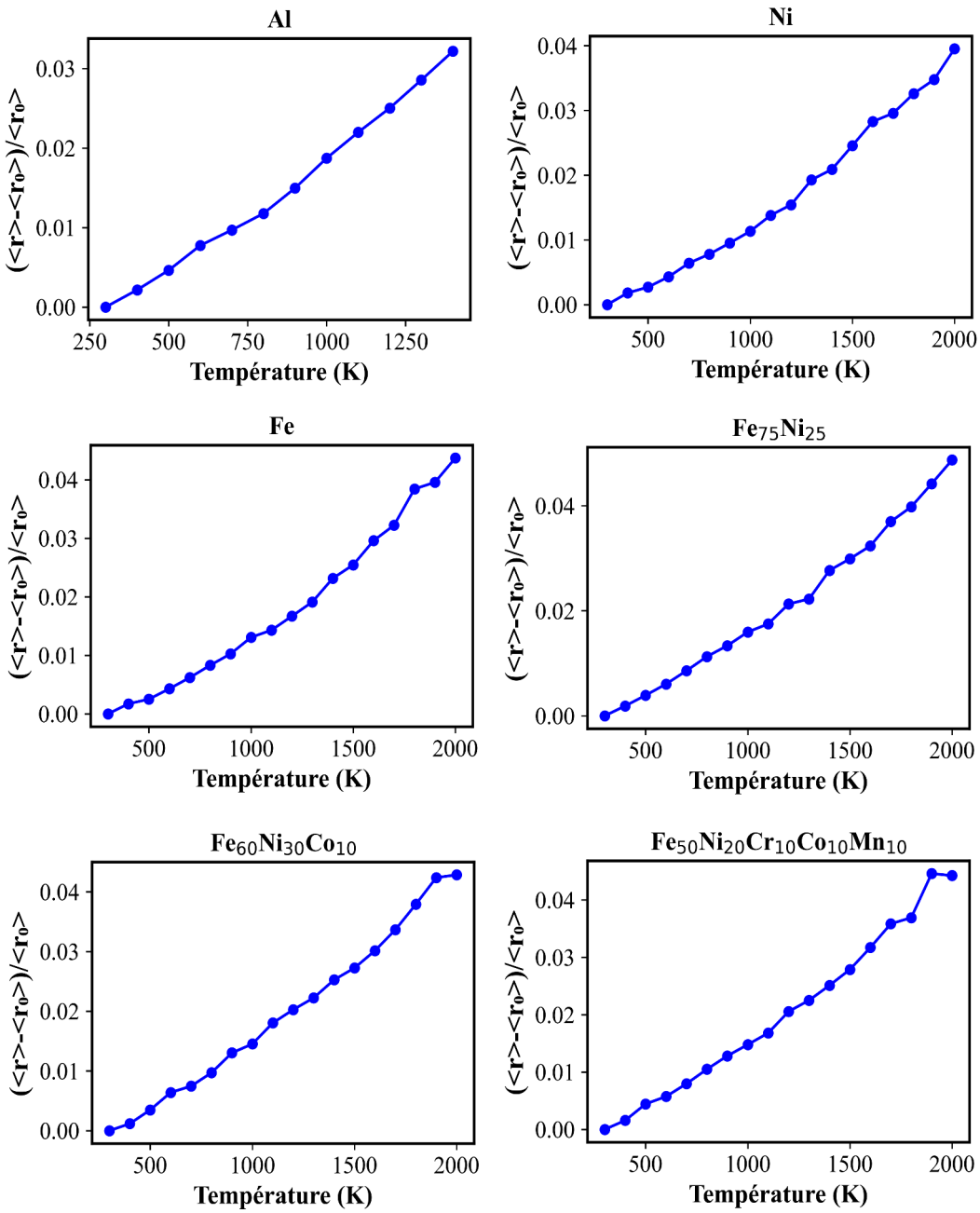

FIG. S12. Relative change of the mean nearest-neighbor distance with temperature for selected systems.